FERMILAB-PROPOSAL-0877 877

Proposal

Measurement of the Magnetically-Induced QED Birefringence of theVacuum and An Improved Laboratory Search for Axions

Siu Au Lee, William M. Fairbank, Jr. and Walter H. Toki
Department of Physics, Colorado State University
Fort Collins, Colorado 80523

John L. Hall
Joint Institute for Laboratory Astrophysics
University of Colorado and The National Institute of Standards and Technology
Boulder, Colorado 80309

Tariq S. Jaffery
Superconducting Super Collider Laboratory
Waxahachie, Texas 75165

Patrick Colestock, Vernon Cupps, Hans Kautzky, Moyses Kuchnir and Frank Nezrick
Fermi National Accelerator Laboratory
Batavia, Illinois 60510

Submitted to
Fermi National Accelerator Laboratory

March 28, 1995

Spokesperson:
Siu Au Lee
Phone: (303) 491-6389
FAX: (303) 491-7947
Email: salee@lamar.colostate.edu

Deputy Spokesperson:
Frank Nezrick
Phone: (708) 840-4604
FAX: (708) 840-3867
Email: frank_nezrick@qmgate.fnal.gov

Measurement of the Magnetically-Induced QED Birefringence of the Vacuum and An Improved Laboratory Search for Axions

Executive Summary

This collaboration has studied the feasibility of a high sensitivity QED birefringence measurement and axion search. The objective of this work is to measure, for the first time, the birefringence induced in the vacuum on a light beam travelling in a powerful magnetic field. The same experimental setup also allows a highly sensitive search for axion or axion-like particles. The experiment would combine custom-designed optical heterodyne interferometry with a string of two SSC prototype superconducting dipole magnets operated at the E-4R site of Fermilab. With these powerful laser tools, sensitivity advances of 10^7 to 10^9 over previous optical experiments will be possible. The proposed experiment will be able to measure the QED light-by-light scattering effect with a 0.1 % accuracy. The increased sensitivity for the axion-two photon interaction will result in a bound on this process rivalling the results based on astrophysical arguments.

In this proposal we address the scientific significance of these experiments and examine the limiting technical parameters which control their feasibility. The proposed optical/electronic scheme is presented in the context of a background of the known and projected systematic problems which confront a serious attempt to make such measurements. Notable challenges arise in the areas of seismic vibration isolation, and the reduction of spurious signals due to background gas contamination and mirror heating. Many delicate choices also must be made for this apparatus to deliver successfully a sensitivity in measuring the change in the index of refraction at the 1.4×10^{-25} level, a domain which the gravitational wave detector groups regard as probable but not guaranteed. The fundamental advantage of our configuration is that our experiment can be configured to be of differential character, in several aspects, thus elegantly suppressing unwanted sensitivities and noise.

We discuss a five year experimental program, with an initial design, construction and research phase of three years duration, during which a 3 m test interferometer and a 50 m large

vacuum optical system will be completed and used for testing. Questions to be addressed during this research phase include: investigation of laser power effect on birefringence of mirrors, development of anti-seismic passive and active suspension systems and mirror control system, demonstration of laser locking of sufficient range and accuracy, development of the laser beam-steering and mirror automatic alignment system, configuration of the magnet string and confirmation of viable magnet ramp rates, beam tube vacuum, and investigation of the light scattering problem and photodesorption of the beam tube. In year 4 full integration of the optical and magnet systems will take place. The 50 m interferometer will be used for initial experiments on the QED effect. In the final year precision measurement of the QED effect will be performed and, in the process, an axion search will be conducted.

TABLE OF CONTENTS

Executive Summary

1. INTRODUCTION 1

2. REVIEW OF THEORY AND SIGNIFICANCE OF THE EXPERIMENT 2

2.1 Magnetic birefringence and dichroism in vacuum 2
2.2 QED birefringence 2
2.2.1 Theory of the dominant magnetic birefringence diagram in QED 2
2.2.2 Higher order QED corrections to magnetic birefringence 4
2.3 Significance of a precision measurement of QED birefringence 5
2.3.1 Comparison to other tests of light-by-light scattering in QED 6
2.4 Search for axions and axion-like particle 10
2.4.1 Axions 10
2.4.2 Magnetic birefringence and rotation due to photon axion mixing 10
2.4.3 Expected sensitivity for axions and axion-like particles 12
2.5 Improvement in the proposed experiment over previous laser experiments . . . 15
2.6 References 17

3. THE OPTICAL INTERFEROMETER 19

3.1 The high finesse Fabry-Perot cavity 19
3.2 The laser source 24
3.3 Seismic isolation and control of the optical interferometer 25
3.4 Birefringence measurement 26
3.5 Results of birefringence data measured with preliminary spectrometer 31
3.6 Rotation measurement 32
3.7 Evaluation of the shot noise limited performance of the interferometer 35
3.7.1 Birefringence measurement shot noise limit 35
3.7.2 Rotation measurement shot noise limit 37
3.8 References 38

4. MAGNET SYSTEM 39

4.1 Magnet system requirements 39
4.2 Magnet selection 39
4.3 Magnetic field issues 41
4.4 Cryogenics requirements 43
4.5 Power system requirements 43
4.6 Quench protection system 45
4.7 Optics and magnet system interface 45
4.8 Technical risks and mitigation 46
4.9 References 46

5. VACUUM SYSTEM 48

5.1 Magnet bore region 48
5.2 Optical chambers 49
5.3 Differentially pumped regions 50
5.4 References 51

6. PHYSICAL PLANT AND ENVIRONMENTAL CONTROLS 52

6.1 Space and environmental requirements 52
6.1.1 Magnet enclosure 52
6.1.2 Optics laboratories 52
6.2 Counting and control room 54
6.3 Cryogenics requirements 54

7. IMPORTANT SYSTEMATIC EFFECTS AND THEIR MITIGATION 55

7.1 Effects of residual gas 55
7.1.1 Cotton-Mouton effect 55
7.1.2 Faraday effect 61
7.2 Effects of seismic motion on scattered light 61
7.2.1 Reflection from pipe walls 62
7.2.2 Motion of beam tube 63
7.2.3 Recommendations regarding scattering 65
7.3 References 66

8. EVALUATION OF PROJECT RISKS AND RISK MITIGATION 68

9. SCHEDULE OF EXPERIMENT 71

9.1 Introduction 71
9.2 Yearly milestones 72

10. DISTRIBUTION OF EFFORT AND COST ESTIMATES 75

10.1 Distribution of responsibilities 75
10.1.1 Colorado State University and University of Colorado/JILA 75
10.1.2 Fermi National Accelerator Laboratory 75
10.2 Cost Estimates 77
10.2.1 Colorado State University and University of Colorado/JILA 77
10.2.2 Fermi National Accelerator Laboratory 78
10.2.3 Total experimental cost 81
10.3 Funding options for the Colorado State/Colorado costs 82

1. INTRODUCTION

The goal of the experiment is to measure, for the first time, the magnetically induced QED birefringence on a beam of light travelling in a strong magnetic field. The same experimental setup also allows a highly sensitive search for axion or axion like particles. The proposed experiment will be able to measure the QED light-by-light scattering effect at the 0.1% level. The increased sensitivity for the axion-two photon interaction will result in a bound on this process rivalling the results based on astrophysical arguments.

During the preparation of this proposal, members of the Collaboration visited the SSCL to evaluate the SSC dipole magnets in regards to their suitability for the proposed experiment. We have also carried out preliminary experiments to demonstrate the capability of our proposed birefringence measurement scheme.

2. REVIEW OF THEORY AND SIGNIFICANCE OF THE EXPERIMENT

2.1 Magnetic Birefringence and Dichroism in Vacuum

When a beam of light travels in vacuum in a strong external magnetic field **B**, the vacuum polarization process of QED induces a small change in the index of refraction of the vacuum. This effect may be interpreted as light-by-light scattering between an optical photon of frequency ω and a zero frequency photon from the magnetic field (Fig. 2.1). For a light beam traveling in a direction perpendicular to the applied B field and linearly polarized at 45° to **B**, this QED effect leads to a greater phase retardation of the component of polarization parallel to **B**, and results in a small elliptical polarization of the light beam. The interaction of a polarized light beam with axions can also produce a birefringence in the beam, as well as a rotation of the polarization. Thus a precision measurement of the optical birefringence and optical rotation of a laser beam in a strong magnetic field can be used to test QED and to search for axion-like particles.

2.2 QED Birefringence

2.2.1 Theory of the Dominant Magnetic Birefringence Diagram in QED

Nearly fifty years ago, Euler and Heisenberg [1] derived an effective Lagrangian for a constant electromagnetic field in vacuum which includes corrections due to vacuum polarization. To lowest order in the QED correction (Fig. 2.1a), this Lagragian can be written as

$$L_{eff} = \left(\frac{1}{8\pi}\right)(E^2 - B^2) + \left(\frac{2\alpha^2}{45(4\pi)^2 m_e^4}\right)\left[(E^2 - B^2)^2 + 7(E\cdot B)^2\right] \qquad (2.1)$$

(Natural Lorentz-Heavyside units, in which $\hbar = c = 1$ and $\alpha = e^2/4\pi = 1/137$, are used here.) Two decades ago, the dominant term in the magnetically-induced birefringence of the vacuum, representing the light-by-light scattering diagram (Fig. 2.1a), was derived by Adler [2] using the Euler-Heisenberg Lagrangian. The result for the difference in the index of refraction is

$$n_{\parallel} - n_{\perp} = \left(\frac{\alpha}{30\pi}\right)\left(\frac{B}{B_{cr}}\right)^2 \qquad (2.2)$$

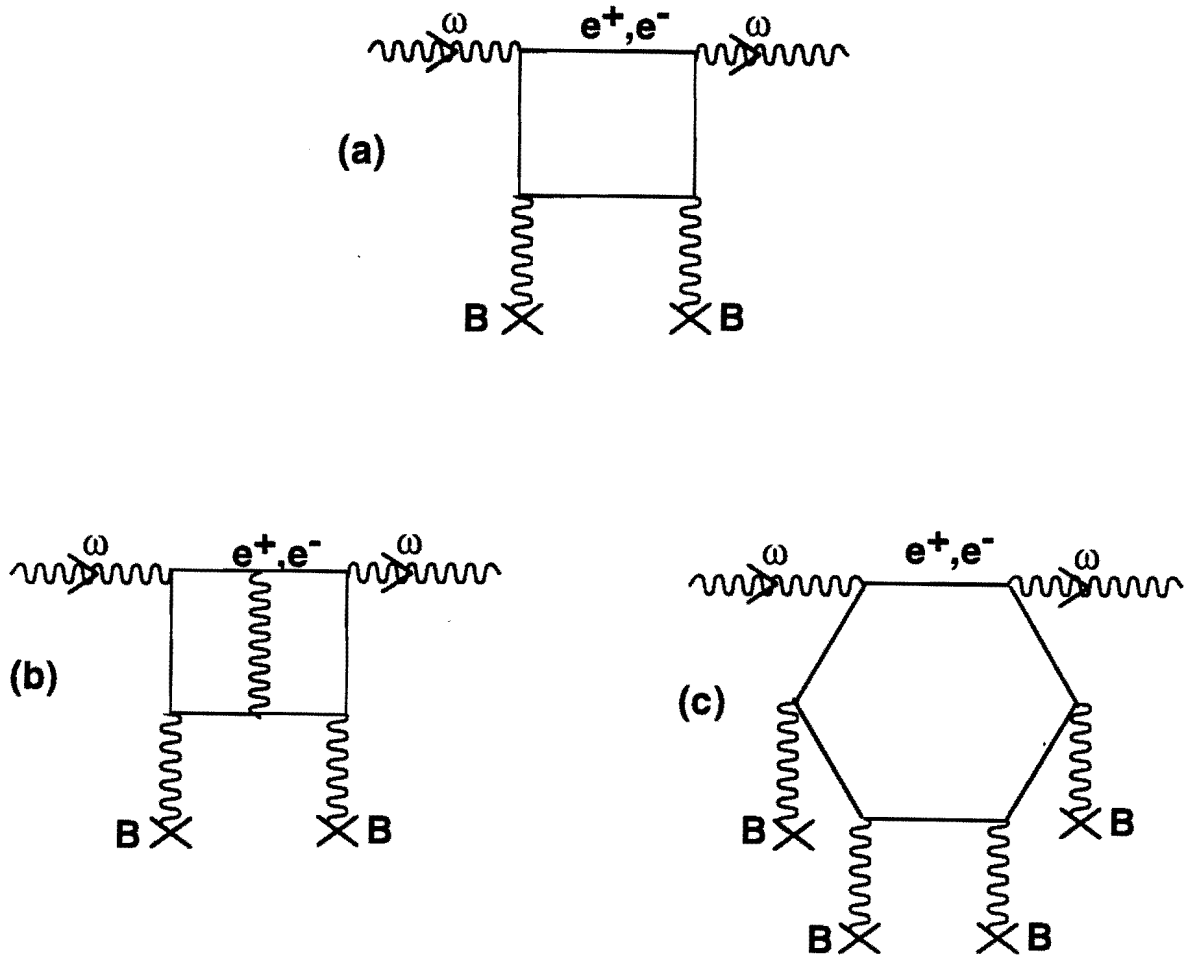

Figure 2.1 Feynman diagrams for vacuum polarization or light-by light scattering producing magnetic birefringence in vacuum: (a) First order diagram, of order $(\alpha/\pi)B^2$. (b) Second order diagram with radiative correction, of order $(\alpha/\pi)^2B^2$. (c) Higher order correction with more magnetic interactions, of order $(\alpha/\pi)B^4$.

where $B_{cr} = m_e^2/e = 4.41\times10^9$ T is the characteristic field at which these corrections become large. The corresponding ellipticity induced in a laser beam polarized linearly at 45° to the magnetic field and making N passes through a field length l, is

$$\psi_{QED} = \frac{(n_{/\!/}-n_{\perp})\,\pi N l}{\lambda} = \frac{Nl}{\lambda}\left(\frac{\alpha}{30}\right)\left(\frac{B}{B_{cr}}\right)^2 \qquad (2.3)$$

where λ is the wavelength of the light. It is quite obvious that in order to observe ψ_{QED}, l, N and B should be as large as possible.

For the conditions of the proposed experiment, $N = 1.33\times10^5$, $B_{eff}^2 = 35\ T^2$, $l = 30$ m, and $\lambda = 532$ nm. Eqs. (2.2) and (2.3) give $n_{/\!/} - n_{\perp} = 1.4\times10^{-22}$ and $\psi_{QED} = 3.3\times10^{-9}$ rad. Although these values are very small, the expected shot noise limit in the proposed experiment is some three orders of magnitude smaller. Thus this QED effect should be not only directly observable for the first time in the experiment, but also a precision measurement of the magnetic birefringence will allow the test of higher order corrections to the effect.

2.2.2 Higher Order QED Corrections to Magnetic Birefringence

Sample Feynman diagrams for the next order corrections to the magnetic birefringence of vacuum are shown in Fig. 2.1b and 2.1c. Radiative corrections such as Fig. 2.1b are expected to be of order (α/π) compared to the dominant diagram Fig. 2.1a. The second order correction to the effective Lagragian, Eq. (2.1) has been derived from the Euler-Heisenberg integral form by Ritus [3]. The result is

$$L_{eff}^{(2)} = \left(\frac{\alpha^3}{\pi(4\pi)^2 m_e^4}\right)\left[\left(\frac{16}{81}\right)(E^2-B^2)^2 + \left(\frac{263}{162}\right)(E\cdot B)^2\right] \qquad (2.4)$$

Notice that, except for different coefficients, this term has a similar form to the dominant first-order Lagragian. Thus it is straightforward to derive an expression for the index difference to second order:

$$n_{\parallel} - n_{\perp} = \left(\frac{\alpha}{30\pi} + \frac{135\alpha^2}{648\pi^2}\right)\left(\frac{B}{B_{cr}}\right)^2 \qquad (2.5)$$

It is interesting that the second-order correction to Δn is predicted to be 1.45% of the dominant term. Thus, the proposed measurement of the QED birefringence to 0.1% will provide a very significant test of these correction terms also. In fact, although light-by-light scattering effects have been observed as small effects in other contexts, the first corrections to these effects have never been seen before.

The contributions from of corrections of higher order in B/B_{cr}, arising from Feynman diagrams of the type shown in Fig. 2.1c, can be derived by further expansion of the expressions given by Adler [2]. The full result for Δn, including the next correction, is

$$n_{\parallel} - n_{\perp} = \left(\frac{\alpha}{30\pi} + \frac{135\alpha^2}{648\pi^2}\right)\left(\frac{B}{B_{cr}}\right)^2 + \frac{11\alpha}{315\pi}\left(\frac{B}{B_{cr}}\right)^4 \qquad (2.6)$$

Since $(B/B_{cr})^2 = 1.8\times10^{-18}$ is extremely small, this correction will be unobservable in the proposed experiment.

2.3 Significance of a Precision Measurement of QED Birefringence

The magnetic birefringence of vacuum has never been observed. Therefore, this experiment provides an exciting opportunity to make a first observation of a new QED effect. Historically such opportunities have been very rare.

Due to the high accuracy which is expected, the proposed experiment also has great importance as a precision test of QED, of which there are also few. The experiment is particularly significant in this regard because it provides the only direct access to the general class of light-by-light (LBL) scattering diagrams. Although contributions from such diagrams have been observed indirectly in several other QED tests, which are discussed below, the next order corrections to light-by-light scattering, which this experiment is expected to measure to the

7% level, have not yet been seen in any experiment.

Theoretically, our proposed new test of light-by-light scattering is also interesting because the theoretical method used to evaluate LBL diagrams leading to magnetic birefringence is very different from that used for g-2 calculations. In the proposed experiment, the predicted effect (2.1) is derived analytically using the effective Euler-Heisenberg Lagrangian of vacuum polarizability [1]. In contrast, only numerical solutions have been achieved for the light-by-light terms in g-2 [4,5].

2.3.1 Comparison to Other Tests of Light-by-Light Scattering in QED

The most precise experimental test of QED is the measurement of the anomalous magnetic moment of the electron, $a_e = (g_e-2)/2$. The current experimental accuracy of 4 parts per billion [4] exceeds that of the fine structure constant, α, by an order of magnitude. At the present level of experimental and theoretical accuracy, 6th order diagrams of order $(\alpha/\pi)^3$, including the lowest order light-by-light (LBL) scattering term (Fig. 2.2a), are tested to the 0.6% level. Due to the uncertainty in α, 8th order LBL diagrams of order $(\alpha/\pi)^4$ (Fig 2.2b) have not yet been tested, although the experimental accuracy is sufficiently great (Table 2.1).

The anomalous magnetic moment of the muon, $a_\mu = (g_\mu-2)/2$, has been measured to the 10 parts-per-million level [5]. Although the precision is vastly inferior to that for the electron, significant tests of 6th order diagrams, including the LBL term to 4.5%, can be made (Table 2.1). This is because contributions from higher order terms are larger in a_μ than in a_e, due to the larger mass of the muon. The present experimental precision is not sufficient for a test of 8th order LBL diagrams, but a proposed 30× improvement in the experiment [6] projects an experimental error comparable to the 10th order LBL term (Table 2.1). Of particular interest in those experiments are possibly observable effects or mass limits for "new physics": gauge bosons such as W_R, Z', Higgs, and SUSY particles, muon or gauge boson substructure, and excited leptons. In addition, although not expected, it is always possible that a fundamental breakdown of QED may occur at some level.

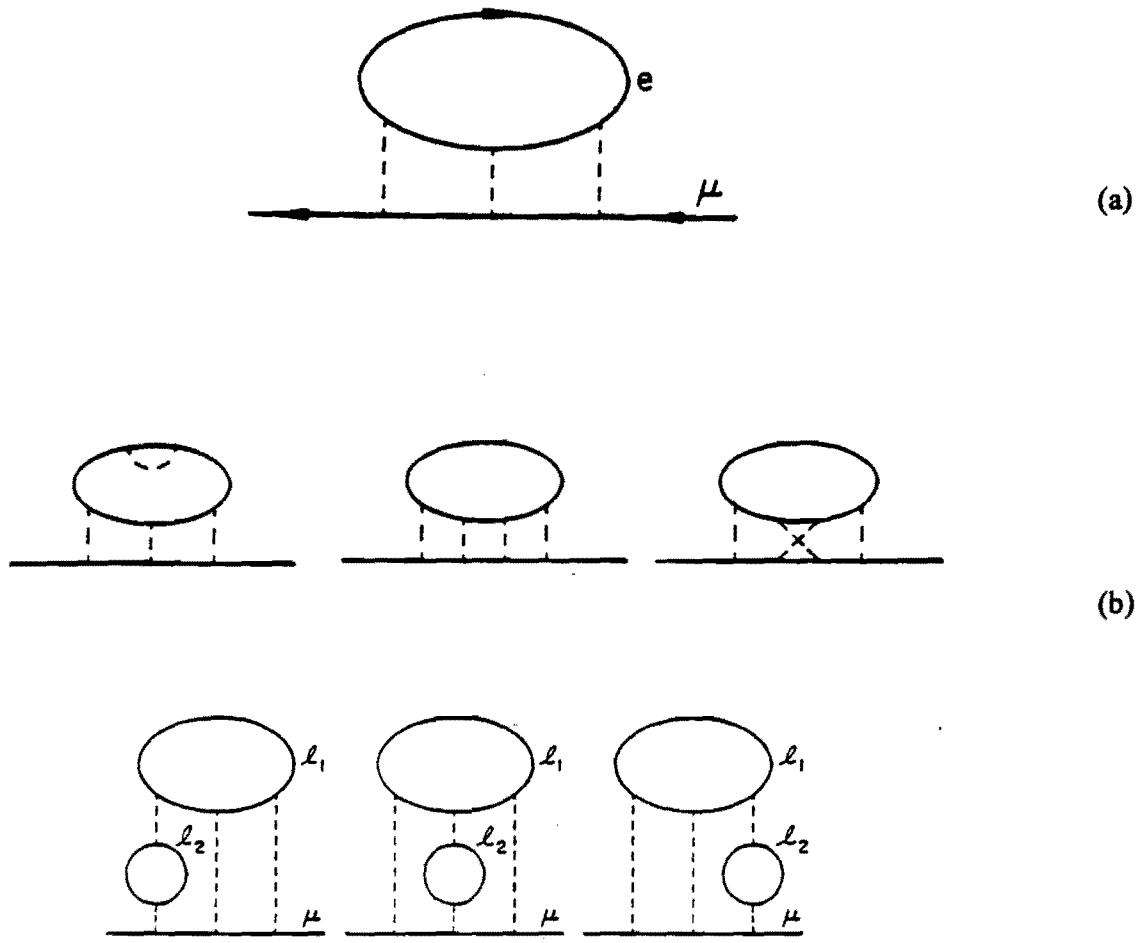

Figure 2.2 Feynman diagrams for (a) sixth and (b) eighth order light-by-light scattering contributions to the electron and muon anomalous magnetic moment.

Our proposed measurement of ψ_{QED} at the 0.1% level is an excellent complement to the electron and muon g-2 experiments. The dominant diagram in the magnetic birefringence effect (Fig. 2.1a) is similar to the 6th order LBL scattering diagram (Fig. 2.2a) which contributes only a small correction to g–2. Thus our experiment provides direct access with comparable precision to LBL terms which are important to know and verify in order to extract "new physics" from g-2 experiments.

A third experiment which probes LBL cscattering more directly is Delbrück scattering of MeV photons off the Coulomb electric field of a nucleus (Fig. 2.3a). Although often complicated by competing Rayleigh, nuclear and Thompson scattering contributions, a measurement of

Quantity	a_e ($\times 10^{-12}$)	a_μ ($\times 10^{-12}$)	**Future BNL expt.**
a_{expt}	1 159 652 188	1 165 926 000	
Δa_{expt}	4.3	12000	400
Δa_{theory}	29 (value of α)	1760 (hadron vac. pol.)	< 400 (better R meas.)
$a_{expt}-a_{theory}$	48 (29)	4820 (12000)	
6th order LBL, $a^{(6)}_{LBL}$	4651 (4)	267 176 (36)	
8th order LBL, $a^{(8)}_{LBL}$	-13.8 (4)	3382 (1)	
10th order LBL, $a^{(10)}_{LBL}$			570 (140)
Hadronic LBL		600(40) (quark) 490 (50) (pion)	
Δa / $a^{(6)}_{LBL}$	0.6 %	4.5 %	0.15 %
Δa / $a^{(8)}_{LBL}$	210 %	350 %	12 %
Δa / $a^{(10)}_{LBL}$		2100 %	70 %

Table 2.1. Contributions to the anomalous magnetic moment a=(g-2)/2 of the electron and the muon.

Delbrück scattering at 2.75 MeV has yielded a test of LBL scattering to 5% [7]. A similar term (Fig. 2.3b) arises as a small correction to the hyperfine structure of muonium. However, the uncertainty in the mass of the muon has precluded a test of this LBL scattering effect [8].

The major experiments which test LBL scattering diagrams in QED are summarized in Table 2.2. It is seen that the proposed experiment, while providing the only clear direct measurement of LBL scattering, is still expected to be competitive with the best previous or planned test of light-by-light scattering in general.

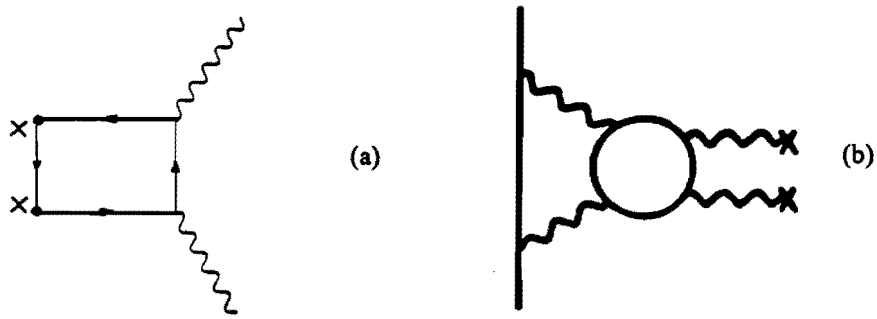

Figure 2.3 Feynman diagrams for (a) Delbrück scattering of a photon off the Coulomb field of a nucleus and (b) the light-by-light scattering diagram for the hyperfine structure of muonium.

Previous Expt.	**LBL term**	**Expt. Error**	**Error / LBL**
Electron g-2 ($\times 10^{-12}$)	4637(4)	4.3 (+29 from α)	0.6 %
Muon g-2 ($\times 10^{-9}$)	271.13(14)	12	4.5 %
Muonium HFS (kHz)	-0.261	0.16 (1.34 from m_μ)	220 %
Delbrück scattering			5 %

Proposed Expt.	**LBL term**	**Expected Error**	**Error / LBL**
Muon g-2 ($\times 10^{-9}$)	271.13(14)	0.40	0.15 %
This experiment	3.3×10^{-9}	3.3×10^{-12}	0.1 %

Table 2.2 Summary of previous and proposed experiments which test light-by-light (LBL) diagrams in QED. The column at the right gives the precision to which LBL contributions to the effect are tested. (The largest error limit is used.)

2.4 Search for Axions and Axion-like Particles

2.4.1 Axions

Axions are light, weakly interacting scalar or pseudoscalar bosons which were hypothesized by Peccei and Quinn [9] to solve the strong CP problem. Various types of axions have been proposed. These include hadronic axions, such as the Kim-Shifman-Vainshtein-Zakharov (KSVZ) axions [10], which couple only to quarks, and Dine-Fischler-Srednicki-Zhitnitsky (DFSZ) axions [11], which couple to fermions. In the standard GUT model and also for DFSZ axions, the axion mass, m_a, and its coupling constant to two photons, $g_{a\gamma\gamma}$, have a specific relation [12]:

$$m_a\,(\mathrm{eV}) \approx 7\mathrm{x}10^9\, g_{a\gamma\gamma}\,(\mathrm{GeV}^{-1}) \qquad (2.7)$$

For hadronic axions, the relationship is the same, except the proportionality constant is $2.7\mathrm{x}10^9$ [12]. Although theoretical interest [13] at present centers primarily on axions near the GUT line specified by Eq. (2.7) on a $g_{a\gamma\gamma}$ vs. m_a plot, it is important to investigate experimentally as large a region of the $g_{a\gamma\gamma}$ vs. m_a phase space as possible in order to exclude or find axion-like particles which may or may not have been theorized to date.

2.4.2 Magnetic Birefringence and Rotation due to Photon-axion Mixing

The theory of the coherent interaction of photons in a light beam with a strong external magnetic field B and low-mass bosons (such as the axion) or leptons has been given by Raffelt and Stodolsky [14]. For brevity, the word "axion" is used loosely in this report to describe all axion-like pseudoscalar particles, and these ideas should be understood to apply more generally. The dominant Feynman diagrams are shown in Fig. 2.4. The Primakoff production term (Fig. 2.4a) leads to a small absorption in the component of the electric field of light parallel to B. This may be observed experimentally as a small rotation of the plane of polarization of the light beam. This process occurs only for axion masses m_a less than the photon energy. The virtual axion

production process (Fig. 2.4b) can take place for $m_a \geq \omega$ or $m_a < \omega$ and leads to a phase retardation rather than an attenuation of the component of polarization parallel to B. This effect induces a small elliptical polarization, and hence a birefringence to the light beam. Both effects are maximized if the incident polarization is at 45° to the magnetic field.

For a light beam polarized at 45° to the B field, the magnetically induced rotation and ellipticity due to photon and axion-like particle coupling are [14, 15]

$$\epsilon_a = N g_{a\gamma\gamma}^2 B^2 \frac{\omega^2}{m_a^4} \sin^2\left(\frac{m_a^2 l}{4\omega}\right), \tag{2.8}$$

and

$$\psi_a = N g_{a\gamma\gamma}^2 B^2 \frac{\omega^2}{m_a^4} \left[\frac{m_a^2 l}{2\omega} - \sin\left(\frac{m_a^2 l}{2\omega}\right)\right], \tag{2.9}$$

where $g_{a\gamma\gamma}$ is the axion-photon coupling constant and $\omega = 2.33$ eV is the photon energy. (In the natural Lorentz-Heavyside units, a magnetic field of 1 T can be expressed as 195 eV^2 and a length of 1 m as 5.07×10^6 eV^{-1}.) Both of these effects are linear in N but nonlinear in l because the axions are not reflected with the photons at the mirrors, and because the axion and the photon do not retain exact phase coherence throughout the interaction region since the axion has a mass. Thus it is seen that a longer length l is a substantial advantage at small m_a ($\varepsilon_a \propto l^2$ and $\psi_a \propto l^3$).

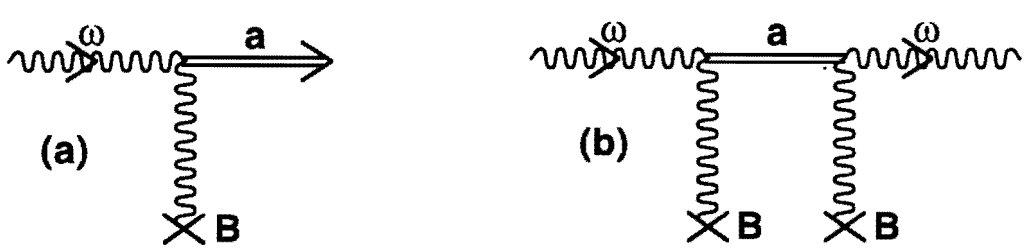

Figure 2.4 Feynman diagrams for axion-photon coupling leading to (a) magnetic rotation and (b) magnetic birefringence in vacuum.

However, much of the advantage is lost for large m_a ($m_a l/2\omega > \pi$) due to the sine functions in Eqs. (2.8) and (2.9). Note that the axion-induced ellipticity ψ_a can be distinguished from the QED induced ellipticity ψ_{QED} through its different dependence upon l. For representative values of ε_a and ψ_a, consider $g_{a\gamma\gamma} = 2\times10^{-10}$ GeV^{-1}. For $m_a \leq 1\times10^{-4}$ eV, the induced rotation from Eq.(2.8) is constant at $\varepsilon_a = 1.0\times10^{-11}$ rad. From Eq. (2.9) we find that ψ_a reaches a maximum value of 1.3×10^{-11} rad (0.4% of the QED value) at $m_a=3\times10^{-4}$ eV. These values are larger than the shot noise limits for a 100 hour measurement, $\varepsilon_{shot}= 5\times10^{-12}$ rad and $\psi_{shot}=3.3\times10^{-12}$ rad. Axions-like particles at this level are therefore expected to be detectable.

2.4.3 Expected Sensitivity for Axions and Axion-like Particles

The limits for $g_{a\gamma\gamma}$ which are expected in the proposed experiment, based on shot-noise limited performance, are plotted in Fig. 2.5. For $m_a < 10^{-4}$ eV the limit from the optical rotation experiment is constant at $g_{a\gamma\gamma} = 1.4\times10^{-10}$ GeV^{-1}. For the optical birefringence experiment the projected limit reaches the value $g_{a\gamma\gamma} = 1.0\times10^{-10}$ GeV^{-1} for $m_a=3\times10^{-4}$ eV, and becomes less sensitive on both sides of this mass. Clearly, the present experiment will not reach the GUT lines representing DFSZ and hadronic axions. Nevertheless, the sensitivity for $g_{a\gamma\gamma}$ is improved by more that three orders of magnitude compared to previous laser experiments [15,16] (due to improvements of 10^7 - 10^8 in ε_a and ψ_a) and by 1.5 order of magnitude over the best previous laboratory experiment in this region, a search for axions produced in the Sun by Lazarus et al. [17]. Although not shown, the solar axion search rules out a roughly rectangular region with $g_{a\gamma\gamma}<4\times10^{-9}$ and $m_a<0.1$eV. The expected sensitivity is also comparable to the astrophysical bounds established from analysis of the evolution of red giant stars [18], $g_{a\gamma\gamma} < 2.4\times10^{-10}$ GeV^{-1} for hadronic axions and $g_{a\gamma\gamma} < 10^{-10}$ GeV^{-1} for DFSZ axions (Fig. 2.5).

A summary of limits from previous searches for axion-like particles, covering a broad axion mass range, is given in Fig. 2.6. While astrophysical arguments appear to rule out GUT axions satisfying Eq. (2.7) for the mass range $m_a>10^{-3}$ eV, only two types of laboratory experiments have had sufficient sensitivity to reach the GUT axion line. These are the telescope search [19], which covers a narrow range 3 eV$<m_a<$8 eV, and particle decay experiments [13],

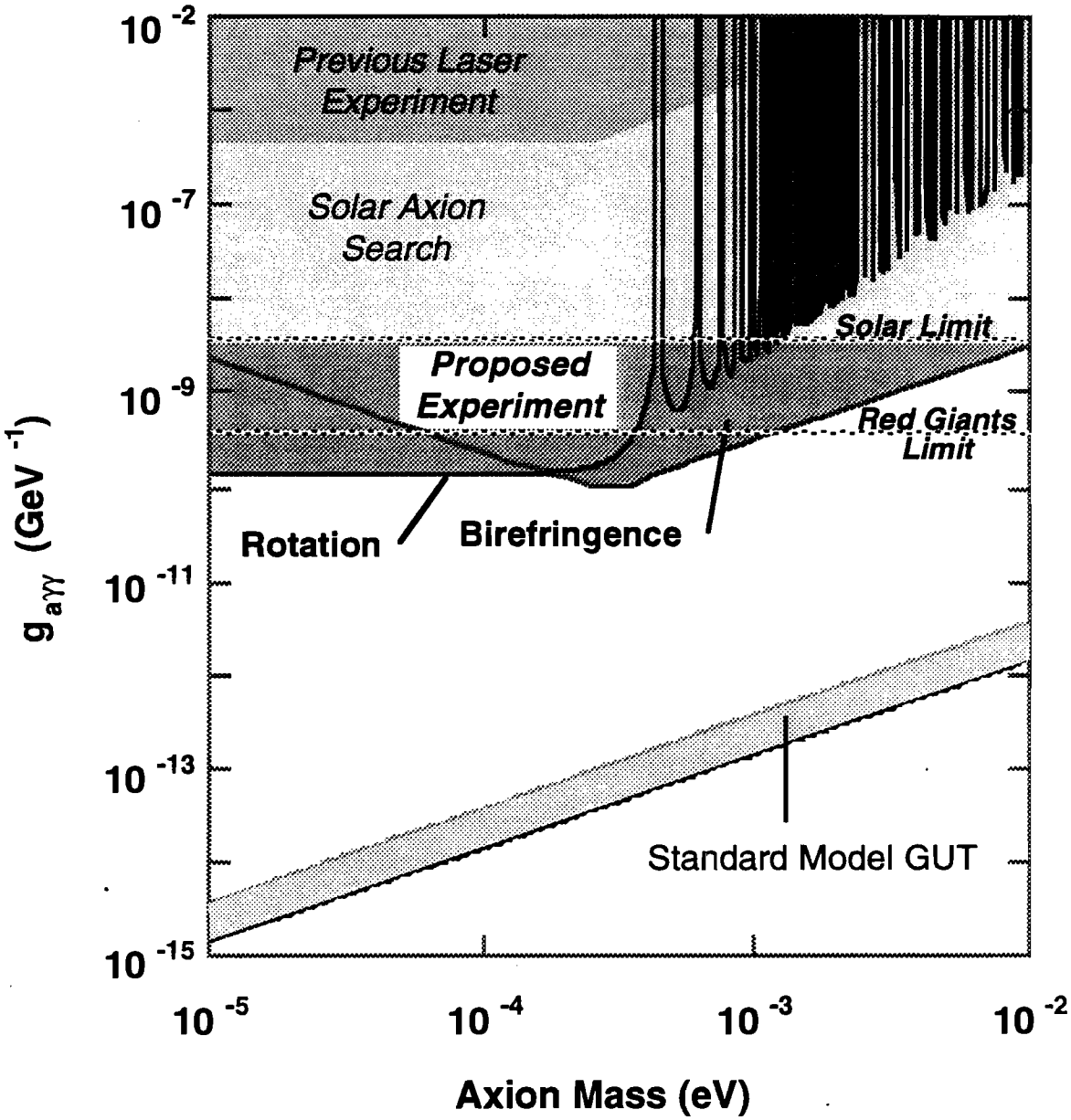

Figure 2.5 The limit on axion mass and axion-two-photon coupling expected in the proposed experiment. For reference, two comparable limits from astrophysical analyses are also presented.

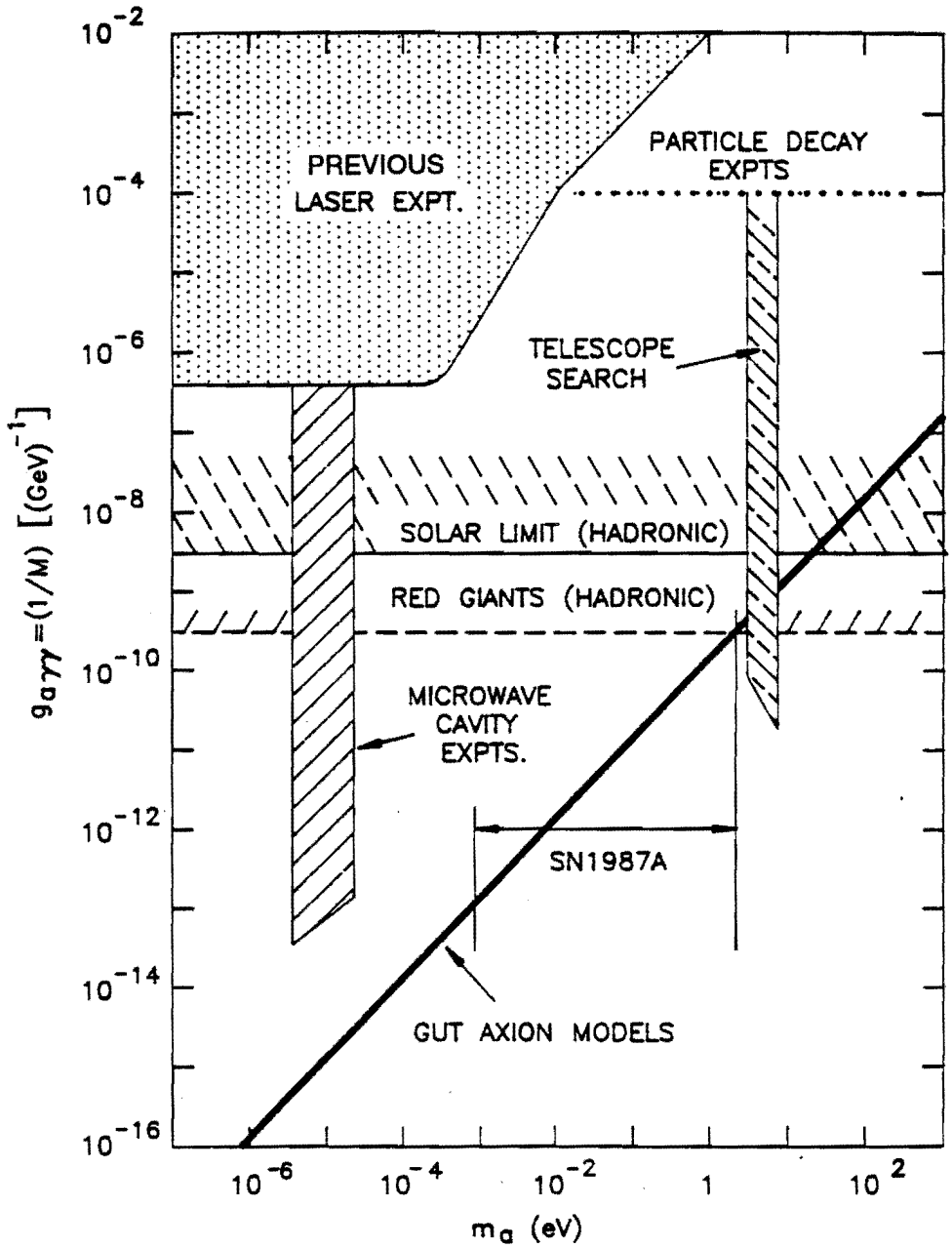

Figure 2.6 Limits on axion mass and axion-two-photon coupling from other experiments and astrophysical considerations. The heavy solid line is the predicted relationship between $g_{a\gamma\gamma}$ and m_a for axions imbedded in GUT models. This figure is reproduced from Ref. 16.

which rule out GUT axions for m_a>6 keV. The microwave cavity experiments of the University of Florida group [20] and the Rochester-Brookhaven-Fermilab group [22], which search for axions in the galactic halo come within a factor of 50 from the GUT axion line in the 4-16 μeV range. Van Bibber et al. [20] have proposed an improved cavity experiment to reach the GUT axion line in this region.

Our proposed experiment will probe a substantial amount of phase space on the $g_{a\gamma\gamma}$ vs. m_a plot (Figs. 2.5, 2.6), which has not been investigated by laboratory experiments. This includes the region $m_a<3\times10^{-4}$ eV, where we expect to establish the limit $g_{a\gamma\gamma}<1.5\times10^{-10}$ GeV^{-1}, and also most of region 3×10^{-4}eV$<m_a<100$ eV, where the limit from the birefringence measurement will improve on previous work.

2.5 Improvement in the Proposed Experiment over Previous Laser Experiments

In order to understand clearly the enormous increase in sensitivity of the proposed experiment over previous optical birefringence and rotation experiments in a magnetic field, it is useful to discuss the best previous experiment in more detail. That is the multipass experiment of the Rochester-Brookhaven-FNAL-Trieste (RBFT) collaboration [15, 16]. In that experiment a Herriott optical delay line cavity is used to reflect the optical beam back and forth many times through the magnetic field region. That method avoids the problem of maintaining resonance conditions in interferometric multipass configurations such as the Fabry-Perot cavity of our proposed experiment. However, the number of passes is not high, the required magnet bore size is large, and reflection spots on the mirrors of the Herriott cavity often come close to the input and exit holes. The latter two problems make that method susceptible to systematic errors associated with scattered light and movement of the mirrors or beam tubes.

The important parameters for our proposed experiment and the RBFT experiment are compared in Table 2.3. The ratios of these parameters, raised to the power that they contribute to ψ_{QED}, ψ_a and ε_a, are listed in the last three columns. The total enhancement factors for the

proposed experiment over those of the RBFT collaboration are listed at the bottom and range from 10^7 to 10^9. It can be seen that the improvement derives mostly from increased signal, rather than more sensitive angle measurements. In fact, the shot noise limit in the RBFT experiment, 4.3×10^{-11} rad, is comparable to that of the proposed experiment. The most significant factors are the large increase in N, arising from the use of a high-finesse Fabry-Perot cavity, and the longer length of the magnet string, made possible by the availability of the SSC magnets. A somewhat larger B field and reduced systematic effects in the birefringence and rotation measurements also contribute significantly to the improvement.

The sensitivity of the RBFT experiment for birefringence was nearly four orders of magnitude short of the predicted QED signal. With an enhancement of 8×10^8 in this experiment, the QED signal will not only be observable, but it can be measured with ~0.1% precision. The expected improvements in the limits for axion-photon coupling, $g_{a\gamma\gamma}$, are the square root of the birefringence and rotation enhancement factors in the last two columns of Table 2.3. The total predicted improvement of 3-4 orders of magnitude in $g_{a\gamma\gamma}$ is consistent with the more detailed calculations in Fig. 2.5.

Parameter	**Previous Experiment**	**Proposed Experiment**	**Enhancement Factors for**		
			ψ_{QED}	ψ_a	ε_a
N_ψ	34	1.33×10^5	3910	3910	
N_a	254	1.33×10^5			520
B^2 (T^2)	4	35	8.8	8.8	8.8
l (m)	8.8	30	3.4	12	12
ψ_{min}	2×10^{-9}	3×10^{-12}	670	670	
ε_{min}	6×10^{-10}	5×10^{-12}			120
Total enhancement factor:			**8×10^7**	**3×10^8**	**7×10^6**

Table 2.3. Important parameters for the previous (RBFT) and proposed optical birefringence and rotation experiments. In both cases the number of passes N and the minimum measurable angle are different between the birefringence and rotation experiments. Thus separate numbers are listed. In columns 4-6 the enhancement factors associated with each parameter are listed. The total at the bottom is a product of individual enhancement factors for each experiment. The improvement factor for $g_{a\gamma\gamma}$ in axion searches is the square root of the listed values.

2.6 References

[1]. W. Heisenberg and H. Euler, Z. Phys. **38**, 314 (1936).
Other derivations have been made by V. Weisskopf in K. Dan. Vidensk. Selsk., Mat.-Fys. Medd. **14**, No. 6 (1936), and by J. Schwinger, Phys. Rev. **82**, 664 (1951).

[2]. S. L. Adler, Ann. Phys. (N. Y.) **67**, 599 (1971).

[3]. V. I. Ritus, Sov. Phys. JETP **42**, 774 (1976).

[4]. T. Kinoshita , "Theory of the Anomalous Magnetic Moment of the Electron - Numerical Approach", in T. Kinoshita, *Quantum Electrodynamics* (World Scientific, Singapore, 1990) p. 218-321.

[5]. T. Kinoshita and W. J. Marciano, "Theory of the Muon Anomalous Magnetic Moment ", in T. Kinoshita, *Quantum Electrodynamics* (World Scientific, Singapore, 1990) p. 419-478.

[6]. Proposed muon anomalous magnetic moment experiment at Brookhaven National Laboratory.

[7]. P. Rullhusen, W. Muckenheim, F. Smend, M. Schumacher, G. P. A. Berg, K. Mork and L. Kissel, Phys. Rev. C**23**, 1375 (1981).

[8]. T. Kinoshita and M. Nio, Phys. Rev. Lett. **72**, 3803 (1994).

[9]. R. D. Peccei and H. Quinn, Phys. Rev. Lett. **38**, 1440 (1977).

[10]. J. E. Kim, Phys. Rev. Lett. **43**, 103 (1979); M. A. Shifman, A. I. Vainshtein and V. I. Zakharov, Nucl. Phys. B**166**, 493 (1980).

[11]. M. Dine, W. Fischler and M. Srednicki, Phys. Lett. **104B**, 199 (1981); A. Zhitnitsky, Sov J. Nucl. Phys. **31**, 260 (1980).

[12]. R. Stryonowski and A. R. Zhitnitsky, "Axion search with optical technique", preprint SMU-HEP-94-12.

[13]. M. S. Turner, "Windows on the Axion", Phys. Rep. **197**, 67 (1990)

[14]. G. Raffelt and L. Stodolsky, Phys. Rev. D**37**, 1237 (1988).

[15]. Y. Semertzidis, R. Cameron, G. Cantatore, A. C. Melissinos, J. Rogers, H. J. Halama, A. Prodell, F. Nezrick, C. Rizzo and E. Zavattini, Phys. Rev. Lett. **64**, 2988 (1990).

[16]. R. Cameron, G. Cantatore, A. C. Melissinos, G. Ruoso, Y. Semertzidis, H. J. Halama, D.

M. Lazarus, A. G. Prodell, F. Nezrick, C. Rizzo and E. Zavattini, Phys. Rev. D**47**, 3707 (1993).

[17]. D. M. Lazarus, G. C. Smith, R. Cameron, A. C. Melissinor, G. Ruoso, Y. K. Semertzidis and F. A. Nezrick, Phys. Rev. Lett. **69**, 2333 (1992).

[18]. G. G. Raffelt and D. S. P. Dearborn, Phys. Rev. D**36**, 2211 (1987).

[19]. M. A. Bershady, M. T. Ressell and M. S. Turner, Phys. Rev. Lett. **66**, 1398 (1991).

[20]. C. Hagmann et al., Rev. Sci. Instrum. **61**, 1076 (1990).

[21]. S. DePanfilis, A. C. Melissinos, B. E. Moskowitz, J. T. Rogers, Y. K. Semertzidis, W. U. Wuensch, H. J. Halama, A. G. Prodell, W. B. Fowler and F. A. Nezrick, Phys. Rev. Lett. **59**, 839 (1987); Phys. Rev. D**40**, 3153 (1989).

[22]. K. Van Bibber et al., "A proposed search for dark matter axions in the 0.6-16 μeV range", LLNL preprint UCRL-JC-106876 (March 1991).

3. THE OPTICAL INTERFEROMETER

A simplified diagram of the proposed optical interferometer for the QED/axion experiment is shown in Fig. 3.1. The output of a Nd:YAG laser is frequency-doubled and sent into an ultrahigh-finesse Fabry-Perot cavity. A strong magnetic field exists in most of the length of the cavity. The input laser polarization is at 45° to the B field. Reflected light from the cavity will be used for birefringence measurements, and transmitted light will be used for rotation measurement. Each of the polarization components parallel and perpendicular to the B field direction is separately locked to its own cavity resonance using the reflected beam. The phase difference between the two polarization components will be measured as a direct readout of the small frequency difference between them. A new scheme of phase measurement is being developed by this collaboration and will be discussed in Section 3.4. Preliminary results obtained to date will be presented in Section 3.5.

The improvement of the present scheme over previous experiments will come from an increase in the number of reflections through the use of the Fabry-Perot cavity ($N \approx 10^5$ instead of 254), a larger magnetic field (effective $B^2 = 35\ T^2$ instead of $4\ T^2$), a longer field region (l = 30 m instead of 8.8 m), a longer averaging time (3.6×10^5 s instead of 655 s), and careful elimination of systematic effects. In the following we will outline the different parts of the optical interferometer and the considerations that go into selecting the parameters.

3.1 The High Finesse Fabry-Perot Cavity

A Fabry-Perot cavity, formed by two mirrors, allows a light beam to reflect back and forth many times through the cavity. The interference between the multiply reflected beams produces the sharp resonances in the frequencies allowed by the cavity. It is important for the proposed experiment that the incoming laser light is in resonance with the cavity. In the Pound-Drever-Hall locking scheme [1], the incoming laser light is frequency modulated such that the fundamental mode is in resonance with the cavity, but the modulation sidebands are reflected by the cavity. The reflected beams are demodulated to provide a feed-back signal for keeping the laser in resonance. The Fabry-Perot resonance condition is given by:

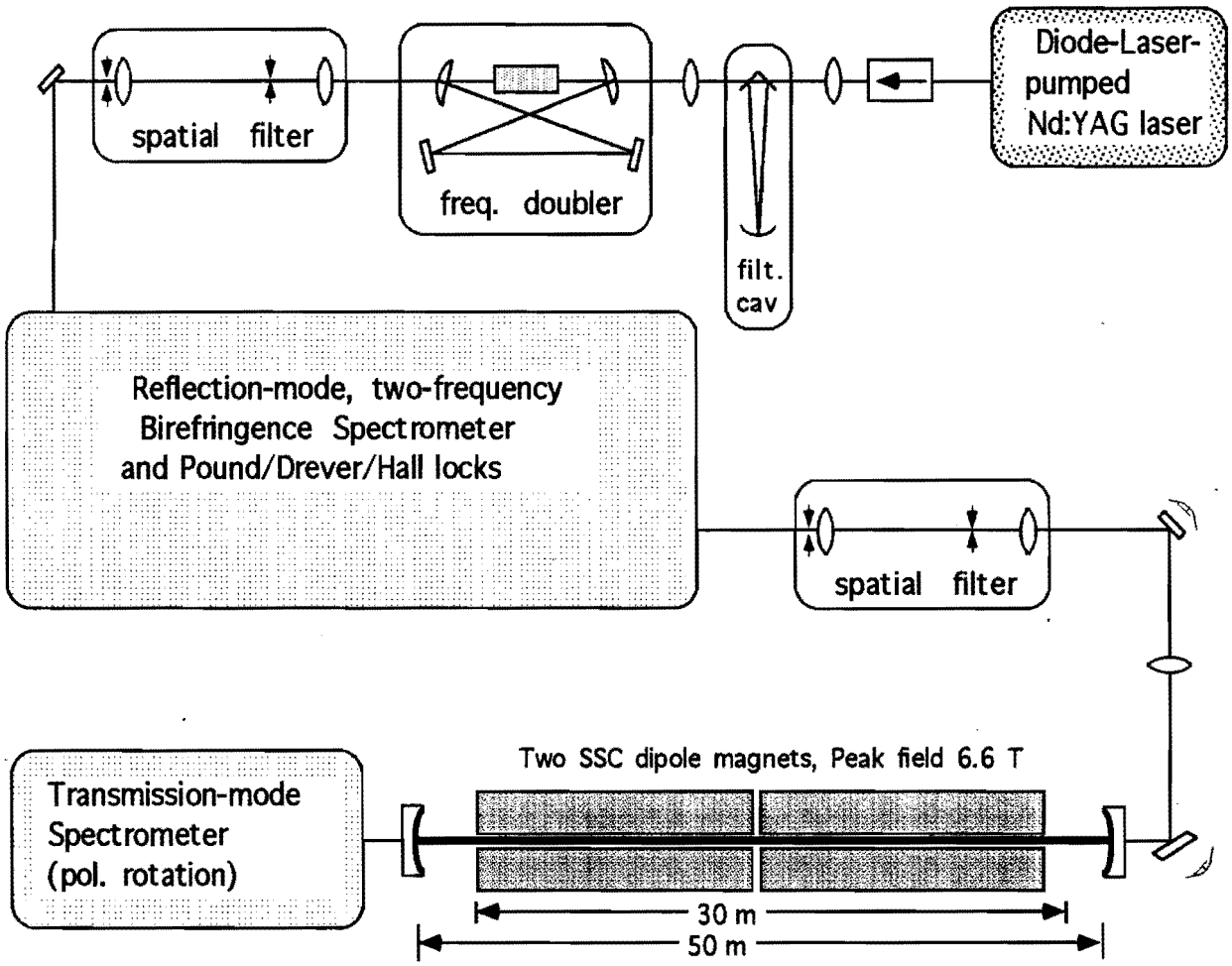

Figure 3.1 Schematic optical configuration of the proposed experiment. The magnetically induced birefringence due to QED effects will be measured with a reflection-mode spectrometer, while rotation of the polarization of the light from possible axion induced effects will be measured with a transmission mode spectrometer.

$$\frac{2\pi}{\lambda} 2nL + \phi_c = 2m\pi \tag{3.1}$$

where m is an integer, n is the index of the medium in the cavity, L is the length of the cavity, λ is the vacuum wavelength of the light, and ϕ_c is any other accumulated phase shift such as due to mirror reflection phase shift and birefringence or laser higher-order spatial modes. There is an additional constant phase due to diffraction. The resonance condition basically states that the total phase increment acquired through one round trip of light travel in the cavity should be equal to an integer number of 2π's.

On resonance, both the transmitted beam out of the back mirror and the reflected beam from the front mirror carry the phase information of the multipassed light beam. In the proposed experiment, the light will be polarized at 45° to the magnetic field direction. Since the // and the $\perp$ polarizations will have different refractive indices due to QED and possible axion induced birefringence, the two polarizations will have slightly different resonance conditions. In addition, the intrinsic and mounting-stress induced birefringence in the mirrors will contribute a DC birefringence on the order of a few Hz. If the cavity is in resonance with one of the polarization components, for example the // polarization beam, then the other polarization ($\perp$ component) will be slightly off resonance, resulting in an elliptically polarized beam. The ellipticity (defined as 1/2 the phase difference between the two polarizations) of the reflected beam is

$$\psi = \psi_1 \left(2\frac{F}{\pi}\right) \beta \tag{3.2}$$

where F is the finesse of the cavity (defined as $\pi\sqrt{R}/(1-R)$, R being the mirror reflectivity), ψ_1 is the ellipticity acquired in a single pass through the magnetic field, and β is a constant ≈ 1 and dependent on measurable mirror coating parameters. Eq (3.2) is written in such a form as to illustrate that the equivalent number of reflections in a Fabry-Perot cavity is

$$N \approx 2\frac{F}{\pi} \tag{3.3}$$

Thus a large number of passes may be achieved with high finesse, i.e., a high mirror reflectivity. At the same time the scattering and absorption losses must be small enough to allow enough

transmission through the cavity.

Considerable progress has been made in recent years in the development of high quality super-polished substrates with surface roughness at the Angstrom level, and in the growth of extremely low-loss thin-film dielectric coatings. Interferometer mirrors with total scattering and absorption losses below 5×10^{-6} are now commercially available [2]. To maintain such low losses, a clean environment is needed during the assembly of the Fabry-Perot interferometer. In custom-made, super-polished mirrors with specially fabricated dielectric coatings, the loss is measured to be as low as 1.6×10^{-6}. A Fabry-Perot interferometer with finesse of 10^6 has been demonstrated with these custom-made mirrors, but for a small beam radius of 84 μm [3]. Similar performance should be possible for a long interferometer, provided that the vibration noise of the mirrors relative to the laser wavelength can be reduced sufficiently to maintain such a finesse. However, for the initial design of the interferometer, we will choose a loss figure of 5 ppm for the mirrors. As more experience is obtained with the operation of large cavities, we anticipate that this loss figure may be improved in the future to the 1ppm level. The parameters chosen for our proposed Fabry-Perot interferometer are listed in Table 3.1

The cavity parameters are chosen to minimize the mode size at the entrance and exit ends of the magnet bore. This will reduce the stray light scattering problem, which will be discussed in Section 7.2. The mirror radius of curvature is fixed by the mode size and the length of the cavity. The mirror diameter is determined from diffraction loss considerations. For the proposed interferometer, the diffractive loss for a TEM_{00} laser beam is estimated to be less than 10^{-13} for a 2" diameter mirror [4]. The finesse of the cavity is chosen to be sufficiently high to allow detection of the QED induced birefringence and from considerations of state of the art mirror technology as mentioned above. The free spectral range of this cavity is 3 MHz and the resonance peaks have a full width at half maximum of 14.4 Hz. Thus it is imperative that the laser source should be pre-stabilized in frequency to less than the cavity width and that ground vibrations are isolated. The vibration isolation of the interferometer mirrors and the associated optics of the birefringence and rotation spectrometers will be discussed in Sections 3.3 and 5.2.

Total length of interferometer L	50 m
Total magnetic field region l	30 m
Mirror loss	5×10^{-6}
Mirror transmission T	1×10^{-5}
Total length of interferometer L	50 m
Total magnetic field region l	30 m
Mirror reflectivity R	0.999985
Mirror transmission T	1×10^{-5}
Finesse F	2.09×10^{5}
Free spectral range	3.0 MHz
Cavity fringe full width half max	14.4 Hz
Maximum intracavity circulating power	5 kW
Mirror radius of curvature	34 m
Mirror diameter	5 cm (2")
Confocal parameter z_o	15 m
Minimum waist radius at 532 nm w_o	1.6 mm
Mode radius at mirror w	3.1 mm
Finesse F	2.09×10^{5}
Free spectral range	3.0 MHz
Cavity fringe full width half max	14.4 Hz
Maximum intracavity circulating power	5 kW
Mirror radius of curvature	34 m
Mirror diameter	5 cm (2")
Confocal parameter z_o	15 m
Minimum waist radius at 532 nm w_o	1.6 mm
Mode radius at mirror w	3.1 mm

Table 3.1 Parameters for the 50 m Fabry-Perot interferometer.

We have found in our laboratory that the intrinsic and stress-induced birefringence in the mirror coatings may be several orders of magnitude larger than the effects that we plan to measure. Indeed this static birefringence is expected to produce a slight offset of ~Hz in the resonance frequencies of the // and the ⊥ polarization components. An important question to investigate is how stable are the value and the eigen-directions of the intrinsic birefringence. The problems associated with static mirror birefringence and its power dependence will be discussed in more detail in Section 3.3. The rationale for limiting the intracavity circulating power to 5 kW will be discussed in Section 3.4.

The magnetically induced birefringence and dichroism in the coatings and the substrates are predominantly linear in the magnetic field, and in principle can be distinguished from the B^2 dependence of the signal by reversing the direction of the magnetic field. Nevertheless, it will be necessary to shield the stray B field to about 1 μG in the optics chambers. The residual gases in the magnet bore region are more troublesome, since their induced magnetic birefringence and rotation effects (the Cotton-Mouton and Faraday effects, respectively) are indistinguishable from the signal. These will be considered in Section 7.1.

3.2 The Laser Source

Important considerations for the choice of a laser source are the available power, the wavelength, and the stability of the output power, frequency, and beam-pointing direction. The experiment requires large number of optical components, and in general, optical materials have lower absorption losses in the visible region than in the UV or IR regions. A larger laser power is desirable for a better shot-noise limited signal-to-noise ratio. Unfortunately high power lasers (>> 1 W) are fairly noisy and do not operate in the shot-noise limited regime. Furthermore, using too high a power in the Fabry-Perot cavity will cause heating of the mirror, resulting in degradation of the mirror performance. Diffraction loss, arising from the finite size of the vacuum beam pipe and mirror diameter, scales exponentially with the laser wavelength and is substantially less important for visible wavelengths as compared to infrared radiation.

The fundamental laser will be a 700 mW diode-pumped Nd:YAG continuous wave laser, frequency-doubled to the visible at 532 nm. The Nd:YAG "MISER" laser is commercially available [5], easy to operate and relatively low cost, and it operates near the shot-noise limited regime. In our collaboration, we have developed the techniques [6] and have demonstrated that the frequency of such a laser can be accurately pre-stabilized to tens of milli-Hertz [7] using a filter cavity. This pre-stabilization is more than sufficient to allow locking the laser to the main Fabry-Perot cavity. The filter cavity also ensures the pointing stability of the output beam. The YAG laser beam is then frequency-doubled in a resonant cavity. In our laboratory we are using a temperature-tuned potassium niobate crystal for second harmonic generation and have obtained a doubling efficiency of 65% [8]. After accounting for the associated losses in the various optics used for preparation and modulation of the laser beam, it is reasonable to expect that at least 100 mW of 532 nm light will be available for input to the main Fabry-Perot cavity.

3.3 Seismic Isolation and Control of the Optical Interferometer

Unmitigated seismic motion would contribute to a frequency noise of more than 1 MHz, corresponding to 10^5 resonance linewidths of the main cavity. Therefore it is essential to have some seriously powerful suppression of this *a priori* seismic noise in order for the cavity to remain on resonance. The first step is to use passive isolation. The approach here is along the ones developed by the gravitational wave community and in investigations carried out in our laboratory. All the birefringence and rotation measuring optics will be mounted on inertial platforms which are vibrational isolated from the ground and the interferometer vacuum chamber by passive and active isolation. The cavity mirrors are suspended from the platforms to allow independent control of the tilt and axial motions of the mirrors. The passive seismic isolation ensures that high frequency ground motion is not communicated to the mirror. Although we are still left with rather large motions, the rates are vastly reduced by the pendulum mounting of the mirrors which acts as a mechanical low-pass filter. We can actively damp the pendulum motion to keep the cavity in near resonance with the optical frequency. At this point the mirror motion (~5 pm) corresponds to ~ 4 cavity linewidths, and there is no easy way to do better on the mechanical side.

Current suspension techniques for the laser interferometer gravitational wave projects (e.g., LIGO and VIRGO), using both passive isolation and active controls, are such that a noise level of $\sim 10^{-18}$ m/$\sqrt{\text{Hz}}$ has been achieved for frequencies above 500 Hz [9, 10]. In our own work we focussed on passive and active vibration control extending to low frequencies, using active first stages of isolation to remove the large amplitude excursions present in a less than ideal situation. A factor of $>10^3$ reduction in the vertical motion has been achieved in one system, and a factor of 100 reduction in all six degrees of freedom has been obtained in another setup by our colleagues, down to frequencies of 1 Hz. The tilt noise (from the twisting motion of the mirrors) will cause a degradation of the cavity finesse. We estimate that a 0.1 μm displacement of the beam in each transit is just tolerable to maintain the finesse. The mirror tilt angle will be controlled to better than a nano-radian with the use of active feedback, using either of two recently published approaches [11, 12].

3.4 Birefringence Measurement

This experiment generates unrivalled demands for measurement precision, far beyond that attainable with the best contemporary or even futuristic atomic clocks. The closest previous effort is that associated with the gravitational wave detection projects which are in the construction phase in the US (the LIGO project [9]) and in several overseas collaborations. Like these experiments, we must be sensitive to exquisitely small effective optical phase shifts, $\approx 10^{-12}$ rad. Additionally, in our experiment we need a concept which is robust against seismic perturbations because it would be difficult to modulate the superconducting magnets at kilohertz rates. It is useful to contrast our interferometer design with the laser interferometer design for gravitational wave detection. In our proposed experiment, the slow magnet modulation means that we can use ultra-high reflectivity mirrors and consequently long effective path lengths. In the gravitational wave detector, the signal to be sought is intrinsically of kHz frequencies, thus requiring low storage time (i.e., low finesse) and high optical power.

The most important difference between this experiment and the LIGO project, and the previous RBFT [13] optical experiment is that we will have enough sensitivity to accurately

measure a non-zero physical quantity, namely the magnetically-induced birefringence due to the QED effect, in the presence of an irreducible background birefringence associated with the mirror fabrication and mounting: Our projected accuracy is about 10^{-9} of this background. So it is clear that *only frequency-based approaches* will have the necessary dynamic range and intrinsic calibration stability for this demanding application.

The basic scheme of the birefringence spectrometer is shown in Fig. 3.2. The incoming laser light is split into two paths with orthogonal polarizations. Two acousto-optic modulators (AOM 1 & 2) shift the frequency of the two channels independently. Each channel is frequency modulated with electro-optic modulators (EOM 1 & 2) which operate at different modulation frequencies. The two beams are recombined, sent through a rotatable half-wave plate, and mode-matched into the high finesse Fabry-Perot cavity. Additional optics and modulator are used to provide optical isolation and to ensure the proper polarization states for the laser beam when entering the cavity.

The frequency of each polarization component is separately locked to be on resonance with the Fabry-Perot cavity via the Pound-Drever-Hall FM locking scheme [1]. The frequency difference between the two polarizations is directly proportional to the birefringence, as can be seen from Eq. (3.1):

$$\Delta\nu = \nu_{\perp} - \nu_{/\!/} = \nu_o\left(\frac{\Delta n}{n_o}\right) + \frac{c}{2n_oL}\left(\frac{\Delta\phi_c}{2\pi}\right) \qquad (3.4)$$

Here ν_o is the laser frequency in resonance with the cavity, and n_o is the average index of refraction of the two polarizations. The first term in the right is due to the index difference, $\Delta n = n_{/\!/} - n_{\perp}$, as light propagates in the cavity. The second term is due to other optical phase shift differences. The quantity $c/2n_oL$ is the free spectral range of the cavity. For 532 nm light, the QED birefringence, with $\Delta n/n = 1.4\times10^{-22}$, results in a frequency difference of 80 nHz.

An important attribute of the QED and axion signatures is that they can be configured to

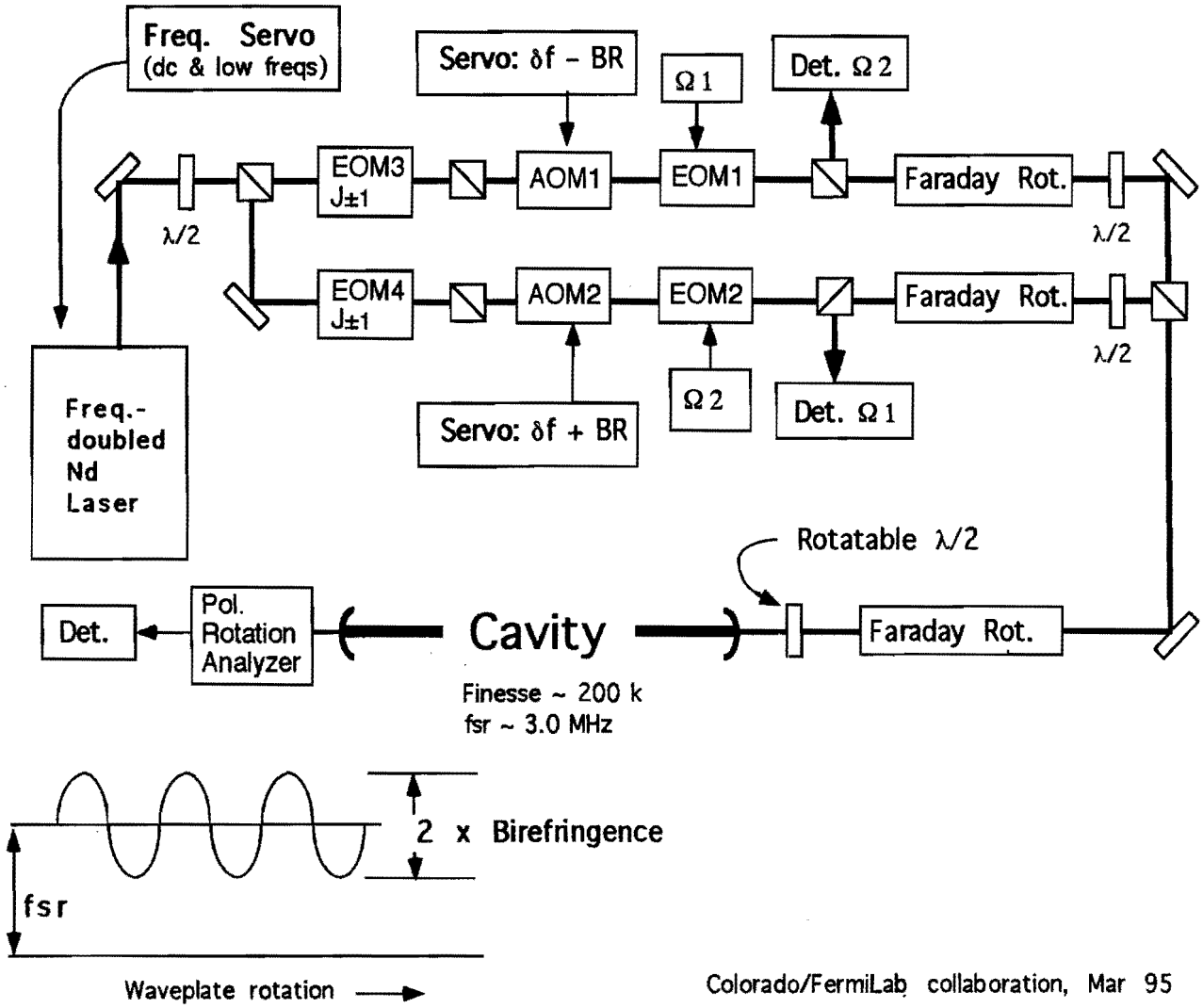

Figure 3.2 The electro-optical measurement techniques for the proposed experiment. A direct measurement of the frequency difference between two orthogonal polarization directions of the laser light gives the QED/axion induced birefringence due to passage of light through a strong magnetic field region in the high finesse Fabry-Perot cavity

produce an optical phase (or intensity) difference between two orthogonal optical polarizations. Suppose the mirrors of our high finesse cavity are such that the principal axes of static birefringence are basically parallel (or perpendicular) to the magnetic field direction to an accuracy of a few degrees. Then the two polarization modes will have slightly different resonance frequencies because of the mirror birefringence. For example, in studies carried out in our laboratory with a 27.7 cm long cavity, the mirrors introduce a phase difference of 3.4 μrad which corresponds to a 300 Hz difference frequency between the two polarization eigenmodes for this short cavity. This work will be described in Section 3.5. Scaling the mirror birefringence value up to the proposed 50 m interferometer, a difference frequency on the order of 1-2 Hz is expected. Our task is to read this ~ Hz beat frequency to an accuracy of < 1 nHz, and to measure the QED induced birefringence changes caused by the magnetic field sweep.

The good news is that because the cavity resonance frequencies of the two polarizations are so nearly equal, any effects due to uncompensated seismic perturbations will be strongly suppressed. However, in Section 3.3, we have found that local opto-mechanical seismic controls will still leave the cavity mirrors with a residual motion of ~ 4 cavity linewidths. Accordingly, we turn to the possibility of shifting the laser wavelength rapidly enough to maintain the resonance accurately enough for the QED or axion birefringence measurement.

We will do this frequency-shifting using two acousto-optic modulators (AOM1 and AOM2 of Fig 3.2), one for each of the two polarization components. In order to satisfy the common-mode suppression of seismic noise, we must shift these two frequencies by exactly the same amount. We also must have these frequencies different as they must match their separate cavity eigen frequencies extremely precisely. The appropriate method to escape this dilemma is to synthesize the rf drive frequencies for the AOMs from a common stem, which includes full seismic compensation of the error signals which are common in the two channels -- this is the seismic signal. The gain of this loop begins at ~100 kHz in our present loops, and tracks out the seismic perturbations to 10^{-4} linewidths with only a pure integrating servo. Using a loop rising faster than 1/f toward lower frequencies leads to an additional factor ~10^3, which is fully sufficient for our measurement, when we recall its differential character.

Tracking the difference in the polarization eigenmode frequencies is an interesting challenge because of the dynamic range and precision requirements already mentioned. Only frequency methods can suffice. We must choose between reading out a servo-defined frequency or generating a precise frequency modulation by Direct Digital Synthesis (DDS), and then testing whether we have chosen the correct amount to match the sum of mirror plus QED birefringence. The latter is our method, in which a measurement iterates with a trial change of the DDS frequency offset, basically forming a stepwise servo system. Because the full birefringence signal has been precisely suppressed nearly exactly (the Hertz level birefringence signal is reduced to within the μHz step size of the DDS), the remaining signal can be digitized comfortably (12 bit resolution is more than sufficient). Calibration of the analog scale is readily accomplished by offsetting the DDS by a few μHz and noting the analog response. The QED signal manifests itself as a field-dependent change in this birefringence readout signal, amounting to a peak to peak frequency difference of 160 nHz .

We now turn to addressing the problems that are likely to arise. In projecting to measure a birefringence change of some 10^{-9} of the mirror's intrinsic birefringence, which in itself is about 1 ppm of an optical wavelength, it is certain that some essential problems with drift will occur. For one, mirror birefringence has been observed to be inhomogeneous spatially, changing by a few percent across a 1" sample. To hold this change to the size of the QED signal implies that the position of the light beam centroid should not move by more than ~50 nm relative to the mirror. This requirement obviously leads to the need for an active angle-steering capability for the cavity illumination. Remembering that the mirrors are mounted via a pendulum suspension, we see that this position servo will need appreciable bandwidth (~ kHz).

An important compromise is involved in the choice of intra-cavity circulating power. Higher power reduces the random noise of the measurement by $\sim 1/\sqrt{P}$, but leads to heating and consequent birefringence due to power absorbed at the ppm level in the mirror coatings. Experience shows that good performance is still possible with circulating power in the 5 kW range, and this will be used as the maximum allowable intracavity power in our design. As better mirrors become available it will be useful to revisit this choice.

As described so far, we would have two optical frequencies applied to the mirror, with a frequency splitting in the Hz range or below. Taken in conjunction with the heating response problem noted above, this small frequency difference clearly will not be a suitable actual choice for doing the measurement. In fact we have already observed interesting polarization-mode interactions at low intracavity powers (< 1 W), which we are presently attributing to photo-refractive type responses at a very low level. So it is necessary to do the locking and data readout with a much larger frequency interval between the two polarization modes. A natural choice is to shift the frequency of one of the polarization by exactly the 3 MHz cavity free-spectral range (FSR) splitting of the long interferometer. This is judged to be an adequate solution with regard to the mirror-heating problem, but costs tremendously in the required performance of the anti-seismic controls. Basically the residual physical motion of the pendulum-suspended mirror now maps into slightly different phase excursions for the two beams, according to their 2.4×10^{-9} difference in wavelengths. An elegant solution to this situation is incorporated into our design with the use of two additional EOMs 3 & 4, whereby one of the polarized beams is split into two equal components, separated by 2 cavity FSRs, one upshifted, the other down-shifted relative to the reference frequency for this polarization. Now the Pound-Drever-Hall lock system produces a cavity-lock signal which is based on the average of the two components. By differentially comparing this with the error signal from the other polarization, the result is free of seismic noise. The exact frequency supplied to these EOM's is not critical (~1 Hz) and can be refined by measurements in an additional rf detection channel as described by DeVoe et al. [14].

3.5 Results of Birefringence Data Measured with Preliminary Spectrometer

A preliminary investigation of measuring small phase differences in a high finesse Fabry-Perot cavity has been carried out in our laboratory. The cavity was a 27.7 cm fixed cavity with a finesse of 4.5×10^4. In this preliminary experiment, the laser was frequency-stabilized He-Ne laser, and the transmitted beam of the Fabry-Perot cavity was used for locking. The optical frequency of the laser was servo-controlled to bring the vertical polarization component to be in resonance with the cavity. The frequency of the horizontal polarization component was brought into precise resonance, however, with the next cavity order by shifting its AOM frequency.

(Thus for this study, the seismic contribution was not common mode and remained an important noise source.) Since there was a small birefringence of ~3.4 μrad present in the mirror coatings, the optical frequencies of the two polarization components differed by 304 Hz (+ one FSR of 541 MHz). Therefore the rf frequencies of the AOMs had to change to maintain both resonances as the slowly rotating half-wave plate exchanged the two polarization states in the cavity. The recorded change in the rf frequency is shown in Fig. 3.3(a). The data show the sinusoidally varying phase changes as the polarization of the incoming light is being rotated relative to the birefringent axes of the cavity.

The available optical power was < 20 μW for each polarization, which corresponds to ~ 6.4×10^{13} photons/s. The relative fluctuation is then expected to be approximately 1.3×10^{-7} with 1 s of integration. In terms of spectral density, analysis leads to a theoretical shot noise limited precision of $1.8 \times 10^{-7}/\sqrt{\text{Hz}}$. With a cavity linewidth of 12 kHz, this theoretical limit is 2 mHz/$\sqrt{\text{Hz}}$. The Fourier distribution of the measured birefringence is shown in Fig. 3.3 (c) for frequencies near the proposed magnet modulation frequency (5 mHz). The present sensitivity is about -80 dB relative to the mirror birefringence of 304 Hz, giving an index of refraction measurement sensitivity $\Delta n/n$ of 6.5×10^{-17}. These first data have a noise level that are many times above the shot noise limit. The noise is in part due to problems of inadequate optical isolation and seismic isolation, and excessive acoustic noise in our laboratory. These problems should be easily remedied. Another important noise source is from the dynamic mirror birefringence which is dependent on the light power and polarization. This is under active investigation in our collaboration.

3.6 Rotation Measurement

In the presence of a strong magnetic field, the creation of real axions from photons would lead to a small absorption of the laser component polarized parallel to the static magnetic field. If the light beam is polarized at 45° to the magnetic field direction, such a preferential absorption of one polarization component would lead to a small rotation in the polarization vector of the recombined beams. In the RBFT experiment [15, 16], the rotation was searched for by using an

(a)

(b)

(c)

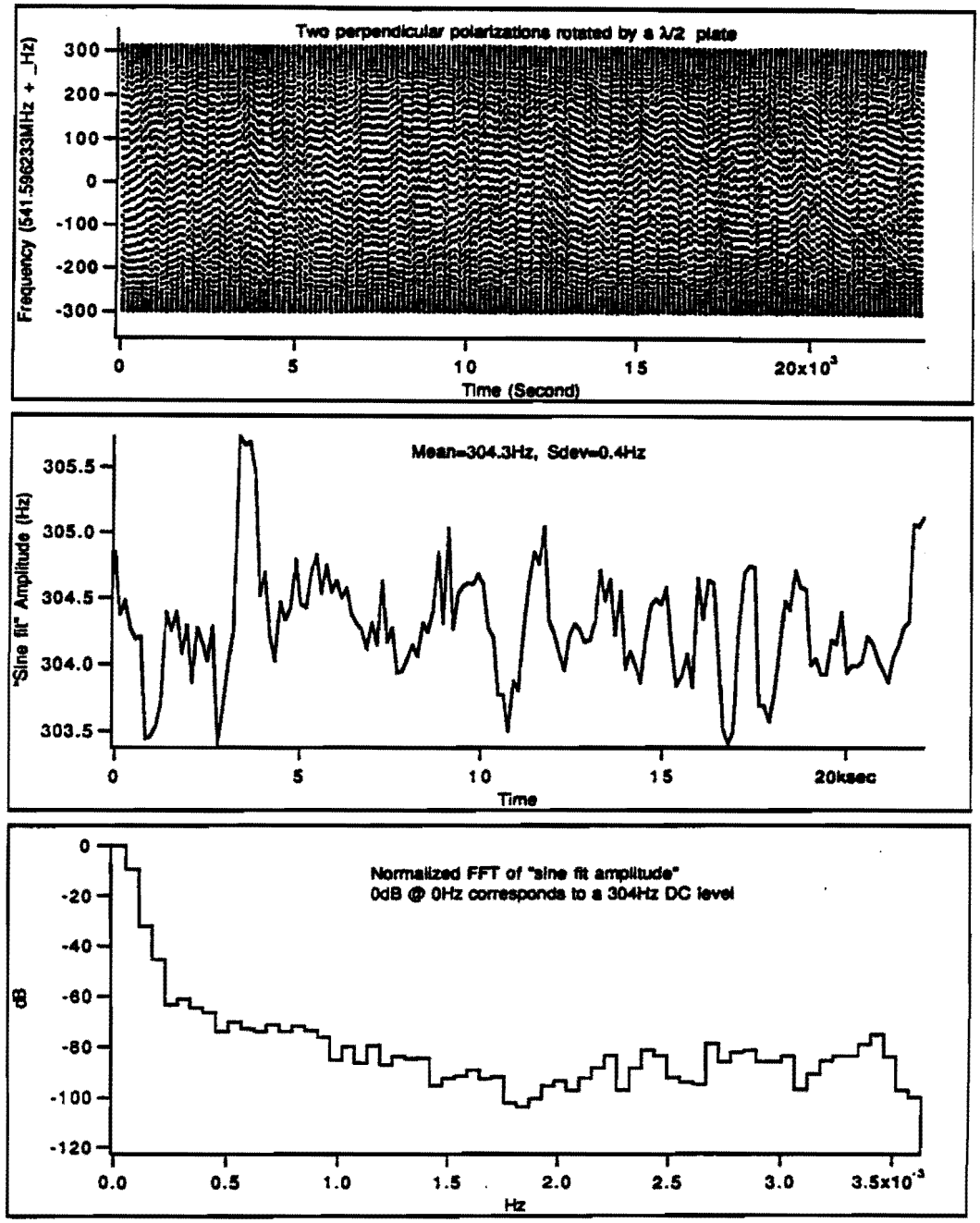

Figure 3.3 Birefringence data measured with preliminary spectrometer.
(a) Time series showing 160 cycles of sinusoidal frequency change between two different cavity eigenfrequencies, dependent upon the rotation of the input linear polarization relative to the cavity birefringence axes.
(b) Amplitude of sinusoid fit to data. Plotted data are fitted cycle-by-cycle, and averaged over four cycles, corresponding to a full 360° rotation of the half-wave plate.
(c) Fourier distribution of measured birefringence. Near our projected magnet modulation frequency, the present sensitivity is about -80 dB relative to the mirror birefringence and is limited by a number of remediable systematic effects.

analyzer whose transmission axis was orthogonal to the original polarization axis of the main beam. A small rotation ε in the polarization leads to a small transmission of intensity ε^2 through the crossed analyzer. In other words the small rotation has "uncrossed" the analyzer. A Faraday cell was used before the analyzer to introduce a much larger, time-dependent rotation $\eta(t)$. Heterodyne detection produces a useful interference term $\eta\varepsilon$ in the intensity which is linear in ε. As in that previous experiment, it is desirable for us to "uncross" the polarization analyzer in an ac manner to produce an ac signal. Our experiment will be enormously more sensitive and a factor of 10^7 improvement is anticipated. (See Table 2.3).

When we examine the transmitted light beam through the cavity, the experimental configuration described above for the QED measurement will produce light beams of slightly different frequencies for the parallel and perpendicular polarizations to the magnetic field direction. Because of this frequency difference, the recombined beam at +45° will show a slow beating, with the detected photocurrent of the form $1 + \cos\delta\omega t$, where $\delta\omega \sim 2\pi \times 2$ Hz is the angular frequency between the two laser beams. The perpendicular choice for the analyzing polarizer will yield $1 - \cos\delta\omega t$. So the "crossed" analyzer does not stay crossed and it is clear that we lose the option to take both birefringence and polarization rotation data simultaneously.

In the axion search experiment then, we will follow the RBFT's method of supplying a single optical frequency polarized at 45° to the magnetic field. Now the crossed polarizer is really crossed and we can employ a magnetic or other polarization dither scheme to achieve the desired heterodyne detection at some frequency of a few hundred Hz as employed by RBFT. One minor difference in our experiment is that the cavity finesse is very high and the two polarization modes will have slightly different resonance frequencies. So the phase of the two transmitted polarization components will be differentially delayed by $\sim 2 \tan^{-1}$ (2 Hz/14.4 Hz) = 0.28 rad or about 16° . However, a stable phase compensator system, such as a Babinet-Soleil compensator, will restore the perfect phase equality. Hence we will still have the very dark null when looking through the crossed analyzer.

3.7 Evaluation of the Shot Noise Limited Performance of the Interferometer

For consideration of shot-noise limited performance, we assume an incident power of 100 mW to the cavity. With mirrors of transmission $T = 1\times10^{-5}$ and loss $L = 5\times10^{-6}$, the power circulating inside the Fabry-Perot cavity is calculated to be 3.9 kW, based on the Pound-Drever-Hall modulation scheme. This power is within the maximum limit established from consideration of the mirror birefringence effect, as discussed in Section 3.4. The transmitted power is P_t = (3.9kW)(T) = 39 mW. The incident and transmitted power values correspond to $N_i = 2.7\times10^{17}$ photons/s and $N_t = 1.0\times10^{17}$ photons/s, respectively. In general we expect the statistical fluctuations to be on the order of $\sqrt{N}$ for a counting type experiment.

3.7.1 Birefringence Measurement Shot Noise Limit

For the QED birefringence experiment, measurements will be made with the reflected beams. In the Pound-Drever-Hall scheme, the incident laser beam is frequency modulated at frequency Ω with a modulation index m, and the incident electric field to the cavity may be written as

$$E=E_i\,[J_o(m)\cos(\omega t)+J_1(m)\cos(\omega+\Omega)\,t-J_1(m)\cos(\omega-\Omega)\,t) \qquad (3.5)$$

where ω is the optical frequency, the J(m)'s are Bessel functions with argument m. Higher order harmonics are neglected in the above equation. The FM frequency Ω is chosen such that, on resonance, only the fundamental frequency (the J_o term) is transmitted into the cavity and the side bands are reflected. In other words, Ω should be much larger than the cavity linewidth. On resonance, the intensity of the reflected fundamental beam is small because of destructive interference, so the photodiode sees a background light mostly due to the sidebands only, $\sim 2J_1^2N_i$. Since the Pound-Drever-Hall scheme is a heterodyne detection scheme, the birefringence signal (measured as a phase in radians) is proportional to the cross term, $2J_oJ_1N_i$. As a first approximation we take the signal-to-noise (S/N) ratio as simply $S/N \approx [2J_oJ_1N_i/(2J_1^2N_i/\tau)^{1/2}] = J_o(N_i\tau/2)^{1/2}$, where τ is the integration time of the experiment. Using a modulation index of 0.5, this corresponds to a minimum detectable birefringence sensitivity (defined as N/S) of 3×10^{-9}

rad/$\sqrt{\tau}$. The QED induced ellipticity per single pass of light beam through 30 m of magnets with B^2 of 35 T^2 is calculated from Eq. (2.2) to be 2.46 x 10^{-14} rad. The total accumulated ellipticity, from Eq. (3.2), is 3.3 x 10^{-9} rad. Therefore this first approximation indicates that 3.6 x 10^5 s (100 hours) of integration will provided a 0.15% QED experiment, if the system is statistically limited.

In an actual optical experiment, we are measuring the current in a photodetector when light is incident on it. For a more exact calculation, the statistical fluctuations due to the random emission of photoelectrons (i.e., the shot-noise) produce a noise current of

$$i_n = \sqrt{2 e i_{dc} \Delta W_B} \tag{3.6}$$

where i_{dc} is the photodetector current, e is the charge of the electron, and ΔW_B is the bandwidth of detection. When the cavity is on resonance, the photocurrent is mainly due to the reflected sidebands and a small amount of residual carrier light from imperfect contrast of the dark fringe. A typical conversion factor between optical power and photocurrent at 532 nm is η = 0.3 mA/mW. Thus on resonance, the photocurrent due to the reflected beam is i = $\eta(P_r)$, where P_r is the reflected power given by

$$P_r = [1 - J_o^2 (1 - R(\frac{1-R-T}{1-R})^2)] P_i \tag{3.7}$$

The slope of the Pound-Drever-Hall discrimination curve provides the conversion from signal photocurrent to optical phase change. A signal current of η $(2J_oJ_1P_i)$ is equivalent to a single pass induced ellipticity of $(\pi/4F)(1-R)/T$ radians. Therefore the shot-noise limited, minimum detectable single pass ellipticity is

$$(\psi_{min})_{BR} = [\frac{\pi}{4F}\frac{1-R}{T}] \frac{\sqrt{2e\eta P_r}}{2\eta J_o J_1 P_i} \quad rad/\sqrt{Hz} \tag{3.8}$$

We also note that the incident power is split equally between the two polarizations. We need to keep track of them separately, and add their shot noise contributions in quadrature. In terms of spectral density, our analysis shows that the shot noise limited sensitivity in the single pass

ellipticity is 3.8×10^{-14} rad /$\sqrt{\text{Hz}}$. (Equivalently, the minimum frequency offset between the two polarization components that can be measured is 120 nHz/$\sqrt{\text{Hz}}$.) Compared to the QED single pass ellipticity of 2.46×10^{-14} rad, a 100 hour integration at the shot-noise limit will be 2.5×10^{-17} rad, which is 0.1% of the calculated QED value.

If, instead of measuring the frequency offset between the two polarizations, we measure the total accumulated phase shift between the two beams, in much the same way as the RBFT experiment, then the shot-noise limited ellipticity on the "output" reflected beam may be calculated from Eq. (3.2) and is 2.5×10^{-9} rad/$\sqrt{\text{Hz}}$. However, the mirror birefringence will also scale the same way and so the measurement technique still needs to have large dynamic range to resolve the QED signal.

Improvements of the birefringence shot-noise limit, aside from going to longer integration time or larger intracavity power, are possible by the use of an asymmetric mirror cavity. In this configuration the transmission and the reflectivity of the two cavity mirrors are purposely chosen to be unequal. If T_1 and L_1, and T_2 and L_2, are the transmission and loss of the input and output mirrors respectively, then the reflected fundamental mode on resonance is completely dark when $T_1 = T_2 + L_1 + L_2$. For example, choosing $L_1 = L_2 = 5 \times 10^{-6}$ and $T_2 = 1 \times 10^{-5}$ as before, the transmission of the input mirror should be 2×10^{-5}. Keeping the same intracavity power, the calculated shot noise limit is improved by a factor of 2. In fact the finesse of this asymmetric cavity, 1.57×10^{5}, is less than the symmetric case, and the incident power required is also less, 88 mW. Thus the asymmetric cavity may be a good alternative to improve the signal-to-noise of the measurement, provided that the mirror transmissions and losses can be matched precisely.

3.7.2 Rotation Measurement Shot Noise Limit

The rotation measurement uses the transmitted beam. Since the scheme of the measurement method is similar to that of the RBFT experiment, the shot noise performance of the system should be similar also. The shot-noise limit calculated in ref. 14 was 4×10^{-9} rad/$\sqrt{\text{Hz}}$. However, in our case the transmitted beam has only a power of 39 mW as compared to their 200

mW. As a rough analysis we expect our shot noise to be some 2.3x higher, and the rotation sensitivity will be ~9 x 10^{-9} rad/$\sqrt{Hz}$. A detailed analysis of our system gives a shot-noise of 1.0×10^{-8} rad/$\sqrt{Hz}$. The sensitivity improvement of the present experiment comes not from shot noise considerations, but from the vastly increased number of passes, a longer B field region and higher field strength, as was discussed in Table 2.3.

3.8 References

[1]. R. W. P. Drever, J. L. Hall, F. V. Kowalski and J. Hough, G. M. Ford, A. J. Munley and H. Ward, Appl. Phys. B **31**, 97 (1983).

[2]. Research Electro-Optics Inc., Boulder, Colorado 80301.

[3]. G. Rempe, R. J. Thompson, H. J. Kimble and R. Lalezari, Opt. Lett. **17**, 363 (1992).

[4]. H. Kogelnik and T. Li, App. Opt. **5**, 1550 (1966).

[5]. Lightwave Electronic Co., Mountain View, Calif., model 122-1064-700F.

[6]. Ch. Salamon, D. Hils and J. L. Hall, J. Opt. Soc. Am. B **5**, 1576 (1988).

[7]. J. L. Hall, to be published.

[8]. A more common crystal for doubling the YAG laser is MgO doped lithium niobate. Although external conversion efficiency as high as 82% has been reported, the crystal tends to degrade with high power. See R. Paschotta et al., Opt. Lett. **19**, 1325 (1994).

[9]. A. Abramovici et al., Science **256**, 325 (1992).
A. Gillespie and F. Raab, Phys. Lett. A **178**, 357 (1993).

[10]. B. Caron et al., "Status of the VIRGO experiment," LAPP-EXP 94-15. S. Braccini et al., Phys. Lett. A **184**, 179 (1994).

[11]. K. Kawabe, N. Mio and K. Tsubono, Appl. Opt. **33**, 5498 (1994).

[12]. N. M. Sampas and D. Z. Anderson, Appl. Opt. **29**, 394 (1990).

[13]. R. Cameron, G. Cantatore, A. C. Melissinos, G. Ruoso, Y. Semertzidis, H. J. Halama, D. M. Lazarus, A. G. Prodell, F. Nezrick, C. Rizzo and E. Zavattini, Phys. Rev. D **47**, 3707 (1993).

[14]. R. DeVoe et al., Phys. Rev. A **37**, 1802 (1988).

4. MAGNET SYSTEM

4.1 Magnet System Requirements

To achieve a satisfactory ratio of signal to noise for this experiment, the dipole magnet system must (1) deliver a high value of magnetic field over a long length, (2) be capable of rapid modulation, (3) have a large aperture aspect ratio (aperture diameter/magnet length), (4) have an aperture tube which can achieve an ultra high vacuum, (5) be reliable and (6) exist as tested complete magnets. Items (5) and (6) are fulfilled by choosing existing SSC dipole magnets. Item (3) is mitigated by choosing dipoles with 50 mm aperture and will be discussed further in Section 7.2. Item (4) is discussed extensively in Section 5.

The individual SSC dipole magnets have been thoroughly tested. Extensive measurements have been made for ramp rate dependence of quench current, AC losses, total heat load, magnetic field transfer function and mechanical behavior. Based on these data the magnet system requirements and characteristics were determined and are presented in Table 4.1. The desired 30 m length of magnetic field will be achieved by using two 15 m SSC prototype dipole magnets. The proposed magnetic field ramping is from 1 T (1000 A) to 6 T (6000 A) at 100 A/s. The magnetic field modulation cycle will be trapezoidal with a 50 s up ramp, 50 s plateau, 50 s down ramp, and a 50 s dwell at 1000 A. The modulation frequency is 5 mHz.

4.2 Magnet Selection

Two 15 m dipoles magnets plus one spare have been selected from the SSC inventory of nearly two dozen prototype dipole magnets. These magnets are DCA207, DCA209, and DCA320. The dominant magnet properties relevant to meeting the six criteria given in section 4.1, are quench performance, ramp rate behavior, and AC losses. Let us consider each of these properties.

The quench current of a magnet is a function of the current ramp rate, the operating temperature, and the amount of cooling (He mass flow). At 4.3 K and 50 g/s He flow, most

Table 4.1 The Magnet System Requirements

Dipole Magnet Length (end plate to end plate)	15.3 m
Desired Field Length	30.6 m
Magnetic Field Modulation	1 to 6 Tesla
Desired Ramp Rate	100 A/s
System Operating Temperature	4.35 K
Dipole Field Measurement Accuracy	< 1%
Aperture Tube Clear Aperture	> 38 mm
System Inlet He Temperature	4.35 K
Length of Magnet Interconnect Region	1.2 m
Inductance per Magnet	76 mH
Power Supply Output Current (max.)	7,000 A
Power Supply Output Voltage (max.)	40 V

SSC prototype dipoles built at FNAL and BNL achieved quench currents in excess of 6000 A at 100 A/s ramp rate. Most magnets achieved quench currents of 5000 A at 250 A/s. Almost all magnets achieved 300 A/s for their down-ramp. The three magnets chosen for this experiment have the quench current vs. ramp rate dependence given in Fig. 4.1. Magnets DCA207 and DCA209 were measured with a He mass flow of 100 g/s while magnet DCA320 was measured at 50 g/s. Note that these magnets have a substantial quench current margin above 6000 A at 100 A/s.

The AC loss, a measurement of the total energy deposited in the magnet during current ramping, is due to the superconductor hysteresis loss, yoke material, and eddy current heating in the magnet coil. For the magnets selected the hysteresis losses are about 740 Joules per cycle and the eddy current losses are about 11 Joules/A/s per cycle giving a total losses per magnet of about 22 Watts at a ramp rate of 100 A/s.

The values of quench current as a function of ramp rate given in Fig 4.1 are for an operating temperature of 4.3 K. If the operating temperature of the magnets is decreased, the quench current will increase by 18%/K. [1].

4.3 Magnetic Field Issues

For the SSC dipoles the transfer function (ratio of magnetic field to coil current) between 2000 A and 5000 A is 1.044 T/kA and linear to 0.1%. At 5 T the iron yoke becomes magnetically saturated. At 6 T the transfer function is lower by about 2%. The magnetic field harmonics of the selected magnets have been measured [2] but are not important for this experiment. The magnets were thermally cycled twice to room temperature and remeasured. There is sufficient data to convince us that the mechanical design of these magnets and the quench performance of these magnets have not been affected by thermal cycles, repeated excitation, and quenching at high currents. It is highly unlikely that continuous ramping of the magnets between 1 and 6 kA will have any ill effects on the mechanical structure and electrical integrity of these magnets.

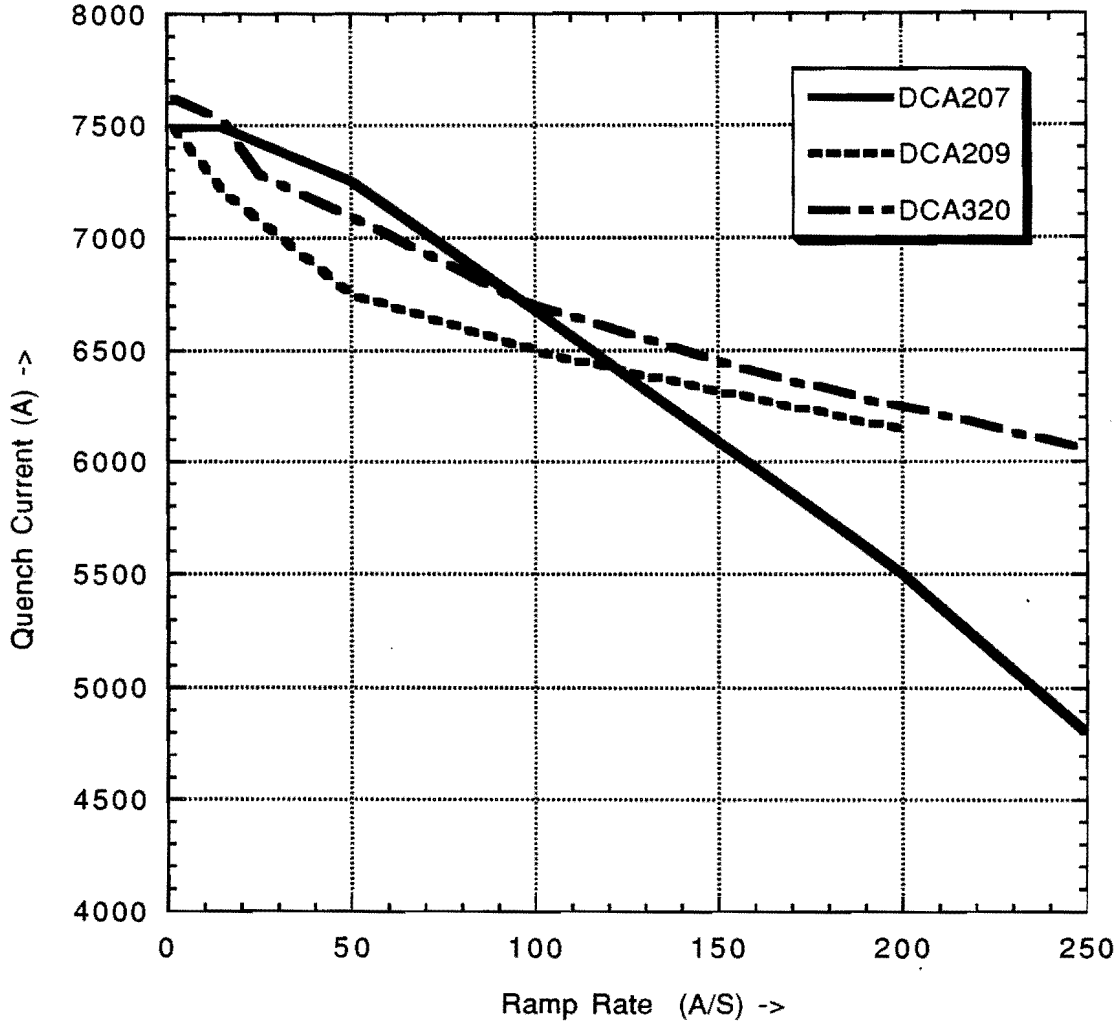

Figure 4.1 Ramp rate dependence of quench current.

4.4 Cryogenic Considerations

The cryogenic system must carry away the static and dynamic heat produced by the modulating magnetic system. Table 4.2 lists the total heat loads for a two dipole magnet system. The heat load values used for the dipoles are from measurements. The head load values for the end cans are based on the Fermilab experience testing 40 mm SSC dipoles at E-4R. The total heat load on the refrigerator, neglecting the transfer lines, is approximately 57 W at 4 K, 22 W at 20 K and 74 W at 80 K.

What will be the operating temperature of the magnets with these heat loads? If all the heat load is transferred to the He, then the temperature rise, dT, across each element is given by

$$dT = Q/mC \tag{4.1}$$

where Q is the heat load of the element (W), m is the mass flow of He (g/s) and C is the specific heat for liquid He at 4.3K (3.95 J/g-K). If the He input temperature is 4.35 K and the mass flow is 50 g/s, then the total temperature increase is 0.02 K across an end can and 0.12 K across a single magnet. The He temperature exiting the second dipole is 4.61 K. This temperature rise appears acceptable for 100 A/sec ramping to 6000 A.

4.5 Power System Requirements

This experiment requires high ramp rates (100 A/s) and continuous cyclic operations between 1000 A and 6000 A for testing and data taking periods of a few weeks to a month with a high degree of reliability. It is proposed to use the Main Injector prototype power supply facility at E-4R to power the magnets in this experiment. The magnet system requires 6000 A at 40 V to meet the requirements given in Table 4.1. This facility, which has operated reliably for several years, can provide a maximum of 9500 A at 1000 V. Water cooled conductors will connect the power supply to the magnet system. It appears that the existing power supply control system is adequate to provide the phase locked current wave form and other controls required for this experiment.

Table 4.2 Heat Loads for a Two Magnet System in the 4 K, 20 K and 80 K Cooling Loops

	4 K	**20 K**	**80 K**
	Watts	Watts	Watt
Magnet System Static Heat Load			
Single Dipole	(1.5)	(5.6)	(37)
Two Dipoles	3	12	74
Feed End Can	5	5	0
Return End Can	5	5	0
Total Static Heat Load	13	22	74
Magnet System Dynamic Heat Load			
Single Dipole	(22)	0	0
Two Dipoles	44	0	0
Total Dynamic Heat Load	44	0	0
Magnet System Total Heat Load	**57**	**22**	**74**

4.6 Quench Protection System

The power supply and quench protection system (QPS) must function together as an integrated system. If a section of the superconducting system starts to go normal, then the QPS senses the impedance change and "disconnects" the power supply from the magnet system and fires the heater firing unit (HFU). The HFU powers heater strips in each of the two magnets which drives both magnet coils normal allowing the quench energy to be dissipated over a larger volume of superconductor. It is believed that with a two magnet system a quench bypass system and a power dump are not required. The experiment will use the existing Fermilab QPS units and the SSC HFUs. Four HFUs must be acquired from the SSC inventory.

4.7 Optics and Magnet System Interface

The beam tube installed in the dipole magnets selected for this experiment has an internal diameter of 42 ± 0.14 mm, wall thickness of 1.3 mm and is made of Armco Nitronic-40 stainless steel. There is no sagitta in these magnets. The cold masses are known to have some sag (~0.02 mm) which is a function of the magnet current [3,4], and the beam tube position can vary within the 50 mm aperture. The anticipated clear aperture is >38 mm, however aperture measurements are required before the magnets are installed in the experiments.

If the problem of photodesorption of H_2 in the beam pipe is serious (see Section 7.1), then additional vacuum pumping and residual gas analysis must be provided at the interconnect region between the two dipoles. This is a contingency plan to be determined by photodesorption tests performed before the installation of the dipole magnets in the experiment.

The magnet system feed and end cans provide the interface volume between the power and cryogenic systems and the magnets. The optical access to the magnetic field region is via the beam tube which passes through the feed and end cans. In the feed and end cans the beam tube has an 80 K shield to minimize heat transfer into the 4.3 K magnet beam tube. UHV gate valves outside the feed and end cans will isolate the cold vacuum region.

The stands designed for these magnets for use at the SSC and for the Fermilab string test are not acceptable for this experiment. For this experiment the magnet stands should provide automatic alignment to give the maximum clear aperture. The stands should also incorporate passive vibration isolation to minimize the noise contribution from light scattered from the magnet beam pipe (see Section 7.2).

4.8 Technical Risks and Mitigation

The major technical risks within the magnet system involve those aspects which can not be evaluated by measurements on individual magnets. Will the magnet system ramp at 100 A/s to 6000 A repeatedly and reliably? Deficiencies in this area can be mitigated by increasing the He mass flow and/or decreasing the temperature of the He input. Does the magnet system have an adequate clear aperture? If the individual elements have an adequate aperture then the system aperture can be optimized by proper and active alignment. Possible misalignments which develop as a function of magnet excitation are more problematic. Risks associated with beam tube seismic vibrations are discussed in Section 7.2. Each of the magnets selected for this experiment will be individually tested at the Fermilab Magnet Test Facility. These magnets will be tested by the Technical Support Section as a part of their program to learn more about lower temperature performance of superconducting dipoles. Part of that testing program will include measurements designed to address the above mentioned concerns.

4.9 References

[1] T. Jaffery et al. "Test Results of Post-ASST design Fermilab-Built 1.5 m SSC Collider Model Dipoles", IEEE Trans. Appl. Superconductivity, **2**, 666 (March 1993).

[2] T. S. Jaffery, M. Wake and W. Kinney, "Automated Methods of Field Harmonics Extraction and Processing for the Magnets in Superconducting Super Collider", presented in International Measurement Technology Conference, Hamamatsu, Japan, May 10-12, 1994

[3] J. Strait et al., "Mechanical Design of 2D Cross-section of the SSC Collider Dipole Magnet", IEEE Particle Accelerator Conference, San Francisco, CA, May 6-9 1991. 4, 2176 (1991).

[4] E. G. Pewitt ed. "50 mm Collider Dipole Magnet Requirements and Specifications", Fermilab 16 Aug. 1991.

5. VACUUM SYSTEM

The vacuum system for the interferometer consists of three regions. The first is the magnet bore region. The second region consists of the two optical chambers which house the interferometer mirrors and the optics for birefringence and polarization rotation measurements. The third region is the differentially pumped sections between the optical chambers and the magnet bore. Several considerations are important for the design of the vacuum system. The residual gas in the magnet bore can produce magnetic birefringence and rotation through the Cotton-Mouton effect and the Faraday effect, respectively. Therefore achieving ultra low vacuum in the magnet beam tube is one of the most critical concerns of the experiment. The requirement of very low scattered laser light necessitates careful consideration of the design and materials for a liner and baffles within the vacuum tube in the magnet bore region. Light traps and additional baffles in the interconnecting region between the magnets and in the interface of the magnets to the optical chambers are also needed. Vibration isolation of the optics and active control of the motion of the interferometer mirrors impact the vacuum in the optical chambers. Shielding the optics from background magnetic fields must also be achieved. Since the three regions have quite different vacuum requirements, each will be discussed separately.

5.1 Magnet Bore Region

The magnet region of the vacuum pipe is cryopumped by the cold bore of the super-conducting magnets. At 4.2 K the only gases remaining should be H_2 and He. Because this region has a large magnetic field, these gases could provide a systematic source of error in the optical birefringence and rotation measurements through the Cotton-Mouton (CM) effect, and to a lesser extent, through the Faraday effect. A birefringence at the shot noise limit, $\Delta n_{shot}=1.4\times10^{-25}$ can arise through the CM effect from a H_2 density of 2×10^5 molecules/cm^3 (1×10^{-13} torr partial pressure at 4.2 K) within the bore tube of the magnets. Thus we will set the design pressure for the magnet region at 1×10^{-13} torr. Although the starting base pressure at 4.2 K in the beam tube can be better than this [1], the base pressure can degrade due to the photodesorption of H_2 by scattered laser light and outgassing from the warmer parts of the vacuum system. The CM effect, the Faraday effect, and the troublesome H_2 problem are discussed in detail in Section 7.1.1. The

conclusions from that section are that the vacuum capability, as these magnets now stand, is far from adequate. These magnets were prototypes and were not prepared to go into an accelerator. The bore was neither heat treated nor polished or coated. A perforated liner with cryosorbing material will be designed to control the H_2 density. The liner can be designed to also act as a light absorber, thereby reducing the multiple scattering of light in the magnet bore. It may be necessary to add pumps in the interconnect region between the magnets to pump out some of the released gas molecules. This is an expensive modification and will be undertaken only if detailed testing indicates it is required.

A larger bore (at least 10 cm in diameter) vacuum tube, containing a Ti sublimation pumping system is to be installed in the interconnect between the dipole magnets. In this section a portion of the gases generated in the cold bore region will be pumped away. If a transition from the beam tube (4 K) to the outside (300 K) is installed in the interconnect region, then a residual gas analyzer will be installed in this region to aid in detecting the photodesorption contamination of the vacuum. Another important role of the large bore tube is to allow light baffles to be placed at properly designed angles so that the pump section acts as a light trap. Our design philosophy is to direct as much of the scattered light as possible into the interconnect regions between the magnets. There the magnetic field is low, absorption of stray light can be efficient on blackened surfaces, and the pumping speed is high. In this way the release of H_2 molecules within the magnet bore regions can be minimized.

5.2 Optical Chambers

The vacuum requirement for the optical chambers is not as stringent as for the magnet bore region. Since the magnetic field will be shielded to a very low value in these regions, the CM and Faraday effects are not a concern. A vacuum of $\leq 10^{-7}$ torr should be adequate to keep the interferometer mirrors sufficiently clean to maintain their low losses and to avoid significant coupling of acoustic perturbations through the residual gas in the chamber .

Each optical chamber will have a 48" diameter by 36" high UHV vacuum chamber, divided into two sections so that the top portion can be raised to allow easy access to adjustments

of the optics housed inside the chamber. This chamber will be anchored to earth. The passive seismic vibration isolation in these chambers probably will be patterned after the mounting system of the LIGO project [2]. As illustrated in Fig. 5.1, all the birefringence and rotation measuring optics are mounted on an inertial platform which is vibrationally isolated within the vacuum from a set of four support beams. The support beam are in turn isolated from the ground by stacks of rubber/steel plate isolation mounts (Fig. 5.1). Soft bellows provide the vacuum seal around the support beams. This passive isolation arrangement ensures that rapid ground motion is not transmitted to the optics and interferometer mirrors attached to the inertial platform. Each interferometer mirror will be suspended from a platform with a means for active control of the mirror's axial and tilt positions. The laser beam enters the vacuum chamber through an optical fiber. It is desirable to have no optical windows between the interferometer mirrors in order to minimize loss and scattering in the high-finesse interferometer cavity.

The optical chambers will be pumped out initially with a turbopump. The operating pressure will be maintained with vibration-free ion and Ti-sublimation pumps. Even with the large number of optical components and associated servo control wiring, a pressure of $\leq 10^{-7}$ torr should be readily achievable in the optical chambers. With specially designed optical components, such as electro-optic and acousto-optic modulators, Faraday rotators, optical mounts and translation stages, and by paying attention to the choice of material for wiring and vibration isolation platforms, it is not unreasonable to expect that a vacuum of 10^{-9} torr can be achieved. The extensive experience of the LIGO and VIRGO [3] projects in this area will be an advantage.

5.3 Differentially Pumped Regions

A transition region must be provided between the room temperature optical chambers at 10^{-7} to 10^{-9} torr and the ultra-high vacuum region ($\leq 10^{-12}$ torr) of the magnet cold bore. This will be provided by a series of differentially pumped sections. The primary concern is molecules which travel down the center of the bore on ballistic trajectories. The mirrors serve as obstacles, blocking the direct paths of gas molecules from the optical chambers to the bore. The gases generated in the interface region will be pumped by small ion pumps and large area getters from

Ti sublimation pumps or other materials. The proper design and performance of this transition region is critical to the success of the experiment.

5.4 References

[1]. William Turner, private communication.

[2]. F. J. Raab, "The LIGO Project: Progress and Prospects," LIGO Preprint PP94-9 (December, 1994)

[3]. S. Braccini et al., Phys. Lett. A **173**, 252 (1993) and references therein.

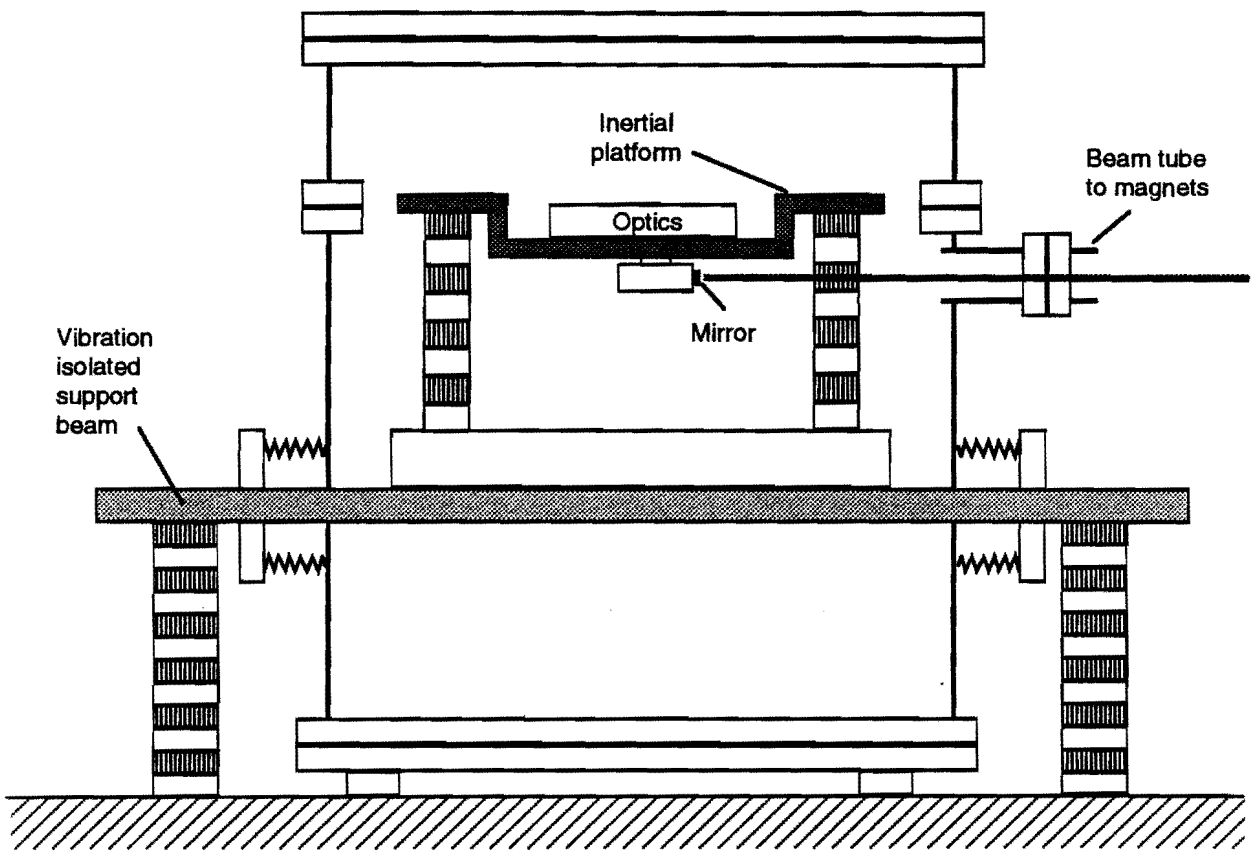

Figure 5.1 Proposed two-stage scheme for passive seismic vibration isolation for the optical platforms at each end of the magnet string. Additional active vibration isolation which may be used is not shown.

6. PHYSICAL PLANT AND ENVIRONMENTAL CONTROLS

6.1 Space and Environmental Requirements

6.1.1 Magnet Enclosure

The two 15 m SSC dipole magnets are housed in a structure composed of 10 Fermilab Main Ring tunnel hoops with a 14 ft wide by 10 ft high hut at the midlength. See Fig. 6.1. Each Main Ring tunnel hoop has internal dimensions 11 ft wide by 9 ft high by 10 ft in length. The end cans because of their height and additional space required for cryogenic U-tube insertion are located in sections which are 14 feet wide by 14 feet high by 20 feet long. These enlarged rooms are also used for ODH ventilation. Ground vibration noises should be kept to a minimum. The temperature of the outside of the magnet system needs to be maintained to better than ±3°C. Electric blankets will be used. There is no requirement on the cleanliness of the air in the magnet enclosure. This area will be an ODH area. The magnet enclosure will be accessed through the optics laboratories.

6.1.2 Optics Laboratories

The optics laboratories will be located at each end of the magnet enclosure. They house the large vacuum optical chambers, the laser and external optics, and vacuum pumping system. The input side optics laboratory will be referred to as optics lab #1, and the downstream optics laboratory as optics lab #2. These two optics labs have different space requirements. Optics lab #1 will be the primary laboratory for the experiment. A clean room of Class 10 will be required for this experiment. Our intent is to use the Research Division Class 10 clean room in the village.

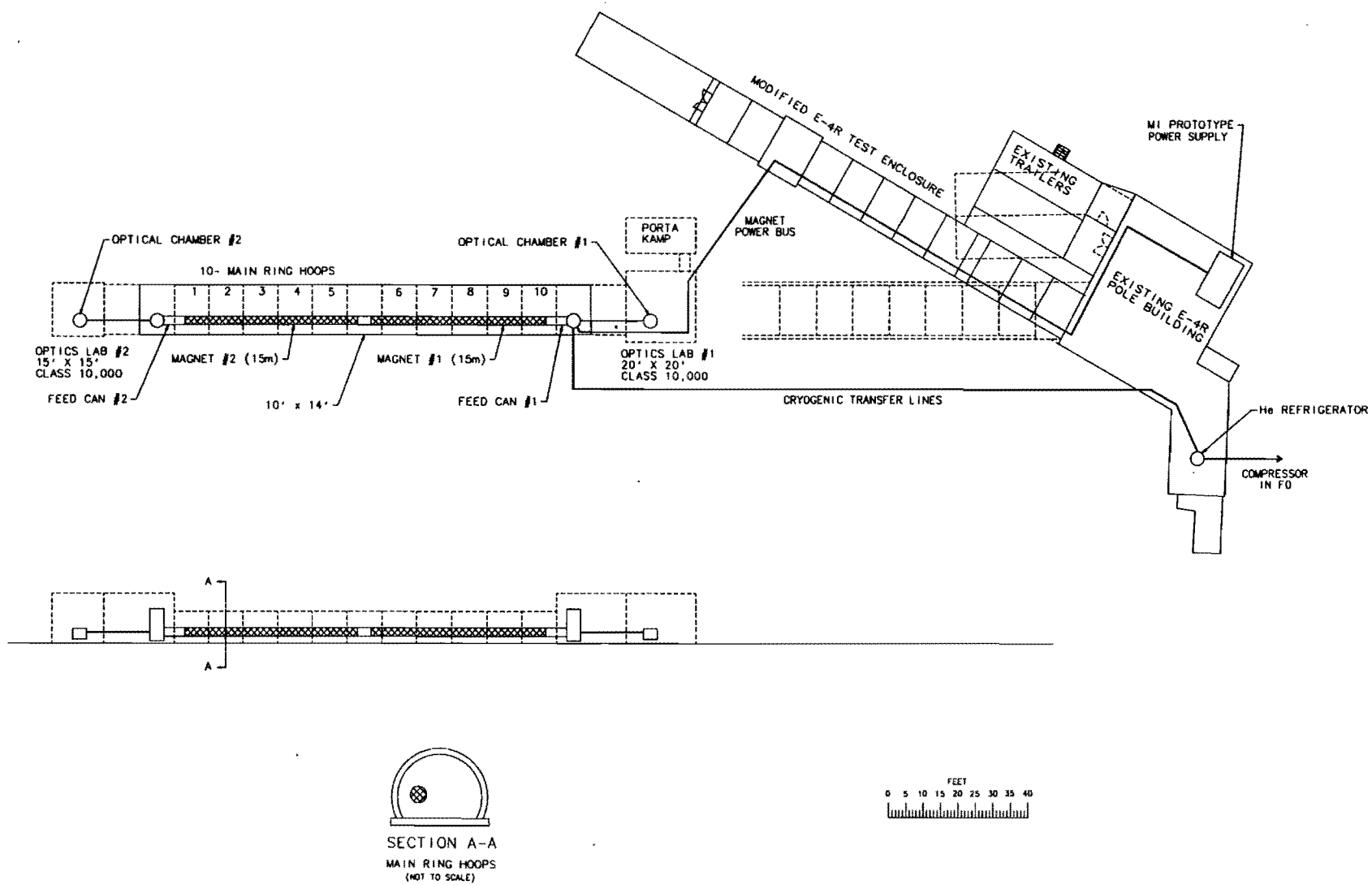

Figure 6.1 Proposed experimental layout at E-4R

Optics Lab #1

Floor Space: Minimum 400 ft^2

Height: Minimum 14 ft high with an 1 ton A-frame crane over the optics vacuum chamber.

Temperature Stability: The temperature of the optics vacuum chamber must be maintained to ± 0.5 °C. Again electric blankets will be used. The beam tube connecting the optics vacuum chamber to the magnet end box must maintain ± 2 °C.

Dust specification: Class 10,000 with controlled accesses to outside areas.

Optics Lab #2

Floor Space: Minimum of 225 ft^2.

Height: Same as for optics lab #1.

Temperature Stability: Same as for optics lab #1.

Dust Specifications: Same as for optics lab #1

6.2 Counting and Control Room

A small counting room is requested which will serve as the location of associated electronics and computers needed for the control of the system and for data collection and analysis. This room will also serve as an environmental intercept between the outside prairie and optics lab #1.

6.3 Cryogenics Requirements

Nominal He flow of 50 g/s at an inlet temperature of 4.35 K and pressure of 4 atm is required. He gas at 20 K and LN_2 at 80 K are needed for maintaining the heat shields of the magnet.

7. IMPORTANT SYSTEMATIC EFFECTS AND THEIR MITIGATION

In Section 3.7, the shot-noise limited performance of the system is calculated. However, systematic effects are clearly a major concern in the measurements. In this section we will analyze the two most important systematic effects, i.e. the residual gas and seismic effects, their contribution to the system noise, and possible mitigation.

7.1 Effects of residual gas

7.1.1. Cotton-Mouton effect

In a strong magnetic field, isotropic substances show a birefringence when light is propagated through them in a direction perpendicular to the magnetic field. This phenomenon is known as the Cotton-Mouton (CM) effect [1]. Experimentally, it is found that the difference in the index of refraction for light polarized parallel and perpendicular to the magnetic field direction is:

$$\Delta n \equiv n_{\parallel} - n_{\perp} = C\lambda B^2 \qquad (7.1)$$

where C is the CM constant, λ is the wavelength of light, and B is the magnetic field. In a gas, the CM constant varies with the gas density and the temperature. For a diatomic molecule, the dependence is $C \propto \rho/T$, where ρ is the gas density, and T is the temperature. The 1/T dependence is due to the thermal agitation of the partially aligned induced dipoles. For gases with spherical symmetry, including monatomic gases such as helium, the Cotton-Mouton constant depends only on ρ.

The Cotton-Mouton effect introduces a magnetic birefringence signal which, for a given gas density, is indistinguishable from the desired QED and possible axion signals. This is a very troublesome aspect, and we consider it to be the most serious of the systematic effects. In principle one can go to as low a gas density as is possible to minimize the CM effect. The SSC magnets have a cold bore at 4.35 K, so that all gases except He and H_2 will be cryopumped

away. This cold bore is a mixed blessing. On the one hand, it is an extremely efficient pumping surface so that the gas density is low. Recent measurements from CEBAF [2] showed that the density is less than 10^6 molecules/cm^3, corresponding to a pressure of 5×10^{-13} torr at 4.2 K. On the other hand, the low temperature in the bore may increase the CM constant significantly. Thus we need to evaluate the density limits allowed for He and H_2, and to consider the mechanism of H_2 production in the beam pipe.

Experimentally measured values for the Cotton-Mouton constant at 0°C and 1 atm are: $C(He) = (3.5 \pm 0.7) \times 10^{-20}$ G^{-2} cm^{-1} with 514.5 nm light [3], and $C(H_2) = (1.9 \pm 2.3) \times 10^{-18}$ G^{-2} cm^{-1} with 546.1 nm light [1]. The calculated value for $C(H_2)$, based on measured electric polarizability and the anisotropy of magnetic susceptibility of H_2, is 1.3×10^{-18} G^{-2} cm^{-1} [1]. We will use the calculated value for H_2 in our estimate, since the experimental result is inconclusive.

The Δn contribution from the CM effect must be kept below the projected experimental shot noise limited sensitivity. For the shot-noise limited 0.1 % QED experiment, $\Delta n = 1.4\times10^{-25}$ for an effective B^2 of 35 T^2. Converting the CM constants for H_2 to 4 K, and using a wavelength of 532 nm, the allowed densities are $\rho(H_2) < 2.1\times10^5$ cm^{-3} and $\rho(He) < 5.2\times10^8$ cm^{-3}. Corresponding partial pressures are 1×10^{-13} torr for H_2 and 2.5×10^{-10} torr for He. Both pressures values are at 4.2 K. (Note that these density values at room temperature will give pressure readings of 4.8×10^{-12} torr and 1.2×10^{-8} torr.) The He does not present a problem unless there is a leak. On the other hand, H_2 is continuously generated in the vacuum system. One source is from outgassing of the stainless steel surfaces in the room-temperature vacuum optical chambers, and the other is from photodesorption as scattered laser light strikes the wall of the cold magnet bore.

The first problem, i.e., outgassing from the room temperature walls, can be mitigated by maintaining an ultra high vacuum $\leq 5 \times 10^{-11}$ torr in the differentially pumped region adjacent to the cold bore. This pressure is within the capability of current UHV technology using Ti sublimation pumps. These will be placed immediately at the two ends of the magnet string to shield the cold bore from the H_2 generated in the warm region. Several differential pumping

stages will allow operation of the mirror and optics chambers in the comfortable ~ 10^{-7} torr domain.

The photodesorption of H_2 can be a serious problem. This is also a real concern for the next generation of large accelerators where significant intensities of synchrotron radiation will be present in the cold bore of superconducting magnets. In our case we are not worried about the heat generated by absorption of scattered light because the photon energy is low. Rather, we are concerned about the density of H_2 in the gas phase. Studies had been carried out for cold beam tube photodesorption effect for the SSCL 20 TeV Collider, at a synchrotron radiation critical energy of 284 eV [4]. Room temperature photodesorption measurements have been performed at CERN for synchrotron radiation having critical energies from 12.4 eV to 284 eV [5]. The CERN study showed that for a baked stainless steel tube at room temperature, the photodesorption yield of H_2 is different from other gases and stays level below 63.5 eV. No data are available below 12.4 eV or at low temperatures. Even though the photon energy is only 2.33 eV in the proposed experiment, photodesorption effect is likely to be important and should not be neglected.

As an estimate we use the measured results and the model calculation of Ref. 4 for 284 eV photons. This will likely be an over-estimate of the effect for 2.33 eV photons. The results of the model calculations of H_2 density versus photon exposure, based on measurements in a 4.2 K cryosorbing beam tube, are shown in Fig. 7.1. The top plot (Fig. 7.1a) is for photodesorbed H_2 with an average velocity corresponding to 4 K. The bottom plot (Fig. 7.1b) is for average velocity corresponding to ~ room temperature, because there is some evidence that H_2 comes off the surface with that velocity. The range of these velocities has quite different consequences for the vacuum requirement. For case (a), there are no surprises. The photodesorption of physisorbed H_2 (component (2) in the figure) will be the dominant contributing factor. If the H_2 density is to be $< 2\times10^5$ /cm^3, the total exposure allowed is about 1×10^{17} photon/m for the Cotton-Mouton effect to become detrimental.

When the Fabry-Perot cavity is in resonance, the total amount of scattered laser light per

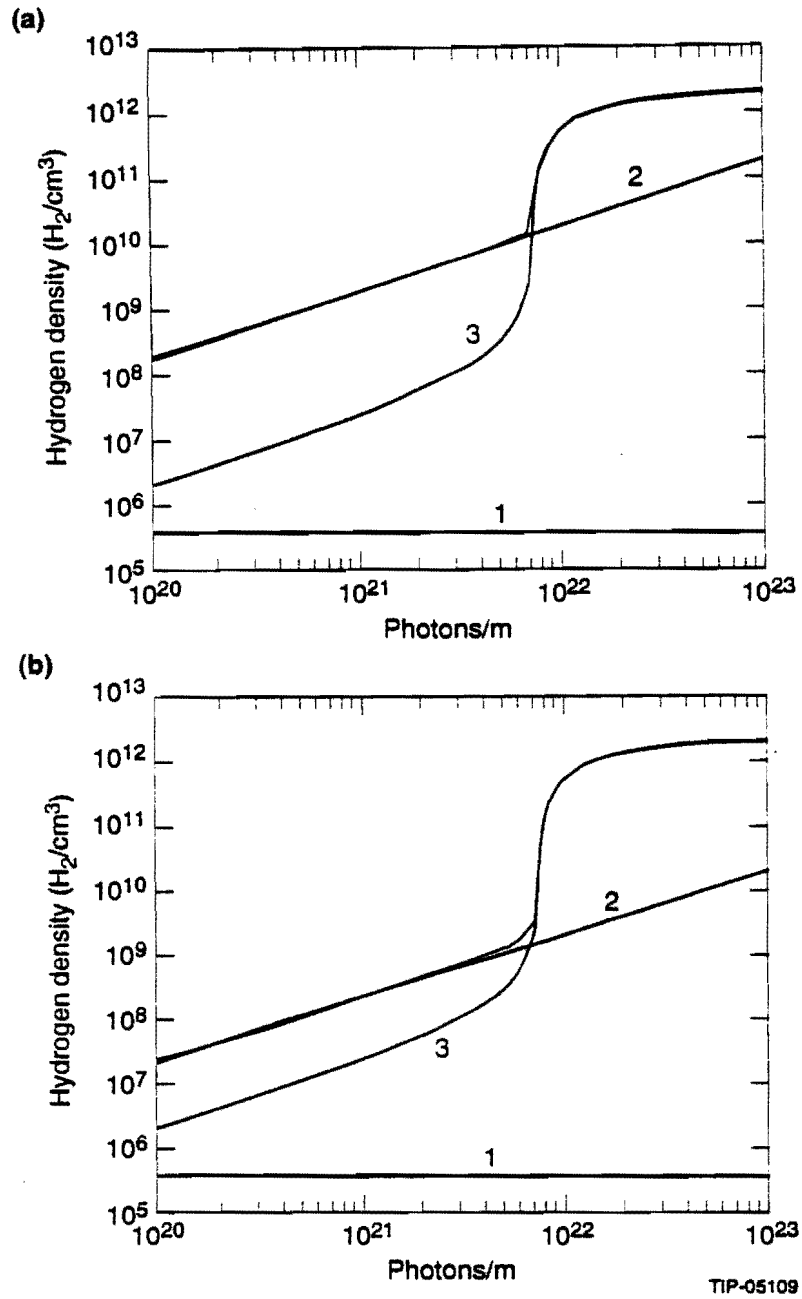

Figure 7.1 Model calculations of H_2 density versus photon exposure in a cryosorbing beam tube; (a) v = 2.1 x 10^4 cm/s and (b) v = 1.8 x 10^5 cm/s. The three density components shown are (1) photodesorption of tightly bound H_2, (2) photodesorption of physisorbed H_2 and (3) the H_2 isotherm. From Ref. 4

mirror for a 4 kW intracavity circulating power and 5 ppm loss on each mirror is 5.3×10^{16} photons/s. Most of this will be scattered into small angles. Using the interferometer geometry, we estimate that the magnet bore will intercept approximately 14% of the scattered light. If this power is absorbed uniformly throughout the magnet bore, the photon flux from scattering by both mirrors is 5×10^{14} photons/s/m. This means that for 4.2 K H_2, we can have a run times of 200 s before the H_2 density becomes intolerable for a 0.1% QED experiment, and then it will be necessary to warm up the bore to pump out the hydrogen. This is certainly unacceptable. Solutions to mitigate the photodesorption of hydrogen in the cold bore region will be described shortly.

Now consider the case of Fig. 7.1b, in which the photodesorbed H_2 moves with room temperature thermal velocity. Since the mean free path is basically the dimensions of the vacuum system, these "hot" H_2 molecules may contribute to the CM effect as if they have a different temperature. Extrapolating Fig. 7.1(b) to the allowable density value of 1.5×10^7 /cm^3 at 300 K, the run time increases to 40 hours.

Because the two results are so vastly different in their impact to the experiment, the velocity distribution of photodesorbed H_2 by 2.3 eV laser light should be measured. Laser spectroscopic techniques, such as two photon or Raman spectroscopy, can be used to measure the velocity distribution unambiguously.

It is also possible to probe the density of the H_2 inside a 4.2 K beam tube using a hydrogen ion beam method [6]. Since at this stage we are unsure of the extent of the Cotton-Mouton "damage", we have listed mitigation for the worst case scenario:

1. Insert a Ti sublimation pumping system in the inter-connect region between the dipole magnets to help pump out some of the desorbed hydrogen. Place a residual gas analyzer (RGA) at the same location to analyze the gas content of the bore. This does not completely solve the H_2 problem. However, if the pressure of the H_2 rises, we expect to see an increase in the birefringence signal. It is then possible to correlate the increase of the signal with the increase of the H_2 density measured by the RGA. Another motivation for putting in a pumping section

in between the magnets is that it will help to mitigate the scattered light problem.

2. Design baffles and light traps so that the scattered light is absorbed in the interconnect pumping regions or in the end feed can region where the magnetic field is low. Pumps will be used to straddle these regions to prevent H_2 from diffusing into the cold bore regions.

3. Use a liner material in the cold bore [7]. The liner is a coaxial perforated tube fitting inside the magnet bore tube and serves two functions: The physisorbed molecules accumulate behind the liner and stay out of view of the photons. The surface morphology of the liner can be shaped (for example, by grooving) to reduce phase noise due to scattered light. Note that in this case there is no need to worry about beam instabilities as in a particle accelerator, so that a liner can be designed with a sufficient number of holes to ensure that the equilibrium H_2 density is kept below 10^6 /cm^3. A partial liner could be formed by sections of high purity graphite which serves the dual purpose as a distributed light absorber and in-situ cryopump of H_2.

4. The SSC magnets were prototypes used for testing and not for actual operation in an accelerator. Therefore the beam tube was not heat-treated or coated. A combination of N_2 glow discharge and 90% Ar + 10% O_2 glow discharge could, for example, be run along the magnet bore prior to cool down to clean the surface of the stainless steel. Studies indicate that this combination appears to be the most effective method in reducing photodesorption and enhancing the lifetime between warmups of the magnet [8].

The implementation of the steps above should allow the lifetime between warmups to be increased to a more reasonable length of time. Note that photodesorption is only important when the Fabry-Perot cavity is actually in resonance. It is not important during most of the testing and setup studies.

7.1.2. Faraday effect

When linearly polarized light propagates through a material in the presence of a magnetic field, there is a rotation of the plane of polarization when the magnetic field has a component along the light propagation direction. This effect is known as the Faraday effect. The angle of rotation of the polarization is given by

$$\epsilon = VlB \tag{7.2}$$

where V is the Verdet constant of the material, l is the length and B is the magnetic field. The Faraday effect will affect the axion measurements but not the QED measurements. Again we will consider H_2 in the cold bore of the magnet. The Verdet constant depends linearly on the gas density. At 0°C and 1 atm, the Verdet constant for H_2 with 578 nm light is $(6.2\pm0.9)\times10^{-6}$ min/cm-G [9]. For an H_2 density of 10^5 /cm^3, the Verdet constant is 6.7×10^{-22} rad/m-G. Therefore the longitudinal B field component in the magnet bore should be less than 50 G to keep the Faraday rotation below the shot noise limit of 3×10^{-17} rad per single pass.

Since the Faraday effect is linear in the magnetic field, the rotation changes sign when the magnetic field direction is reversed. Therefore the longitudinal fringe fields due to the opposite ends of the magnets would cancel out in a first approximation, as would the symmetric sags in the magnet cold mass. Any residual Faraday rotation can be studied by reversing the direction of the magnetic field.

7.2 Effect of Seismic Motion on Scattered Light

Light hitting a mirror may be scattered out of the main beam of the interferometer. This scattered beam may in turn make its way back into the main beam by reflection or scattering off the walls or baffles of the surrounding beam pipes. The scattered beams travel a different path length relative to the main beam and contribute a phase shift to the main beam signal. The scattering phase shift oscillates as the beam pipe is moved from seismic effects and acoustic perturbations. Thus the scattered light contributes a phase noise which can severely degrade the

system performance of the interferometer.

The difficulty of the scattered light problem of the proposed interferometer is similar to that encountered in the laser interferometer for gravitational wave detection (LIGO project [10]). Analytical methods [11] that were developed for the LIGO project will be used here to obtain an estimate of the effect. However, the proposed interferometer has additional electro-mechanical effects. The magnets will change length and flex, in phase with the ramping of the magnetic field. For a complete analysis we also must keep track of the phase evolution of the two orthogonal polarizations. Therefore the light scattering calculations could be more difficult for the proposed interferometer than for LIGO.

7.2.1. Reflection from Pipe Walls

One improtant process for noise generation in the experiment is the recombination of scattered or diffracted light into the main beam mode. For example, light scattered from a mirror travels down the pipe, reflects at least once off the pipe walls, reaches the other mirror, and scatters back into the main beam. Since the reflectivity of the pipe walls are large only at grazing angles of incidence, baffles are used to block the small angles and force the light-beam to reflect at large light-beam pipe angles. In general the light will then have to undergo many reflections as it travels from one end of the pipe to the other. The larger the number of reflections, the more likely the light will be scattered away and be absorbed by the walls of the beam tube.

Ideally the walls and baffles should be deliberately blackened to lower the reflectivity and increase light absorption. The bore tube of the SSC magnets is made of unpolished stainless steel. One solution to decrease the reflectivity is to introduce a liner or sleeve into the bore. The material and surface topology of the liner would be chosen so that the liner becomes a distributed light absorber throughout the bore. The liner also serves to reduce the photodesorption of H_2 in the cold bore - a topic that is important for the Cotton-Mouton effect discussed in Section 7.1.1.

7.2.2. Motion of Beam Tube

An unavoidable source of vibration for the beam pipe is ground motion. The amount of seismic motion is site dependent, and the actual value must be evaluated for the experimental location. Nevertheless it is possible to obtain an estimate of the effect of ground noise. Fig. 7.2 shows the spectral density of power of the vertical seismic displacements measured at a typical magnet testing enclosure (the SSCL site [12]). At frequencies above 100 Hz, the vertical displacement has an approximately $1/f^2$ dependence. The displacement levels off somewhat between 1 - 100 Hz, and increases below 1 Hz due to the microseismic peak. At 1 Hz, the vertical motion is ~ 3×10^{-9} m/$\sqrt{\text{Hz}}$. This type of displacement is fairly typical of a laboratory [13], e.g., see Fig. 7.3. We expect that the horizontal motion is about the same order of magnitude [14].

Analysis from LIGO shows that the phase noise is mainly due to the back scattering from the first set of baffles [15]. The sensitivity limit due to beam tube motion is expressed in terms of the square root of the spectral density of noise h(f), in units of "strain per root Hz". For our experiment, $h(f) = \Delta L/L = \Delta n/n$. The noise is [11,15]

$$h(f) \approx 4\alpha\sqrt{\ln\left(\frac{L}{l_1}\right)}\,\frac{\lambda}{Y}\sqrt{\frac{d\sigma}{dA\,d\Omega}}\,\frac{\xi(f)}{L} \qquad (7.3)$$

The above equation assumes that the scattering probability of main-beam light from an interferometer mirror into unit solid angle around a direction that makes an angle θ with the normal of the mirror follows the form $dP/d\Omega = \alpha/\theta^2$. For our interferometer geometry and a 5 ppm loss mirror, $\alpha \approx 7.8\times10^{-8}$. L is the length of the cavity (50 m), l_1 is the distance from the mirror to the first set of baffles (10 m), λ is the wavelength (532 nm), and Y is the distance from the center of the main beam to the nearest baffle edge, $Y \geq 1$ cm. $d\sigma/dA\,d\Omega$ is the scattering probability from the baffle surfaces, and is ~ 10^{-2} for most wall materials. $\xi(f)$ is the square root of the spectral density of fluctuational displacements of a typical point on a typical baffle. For an estimate we will assume that the beam pipe and baffles are sufficiently well-anchored so that $\xi(f)$ is on the order of the seismic noise. The noise contribution to the sensitivity of the

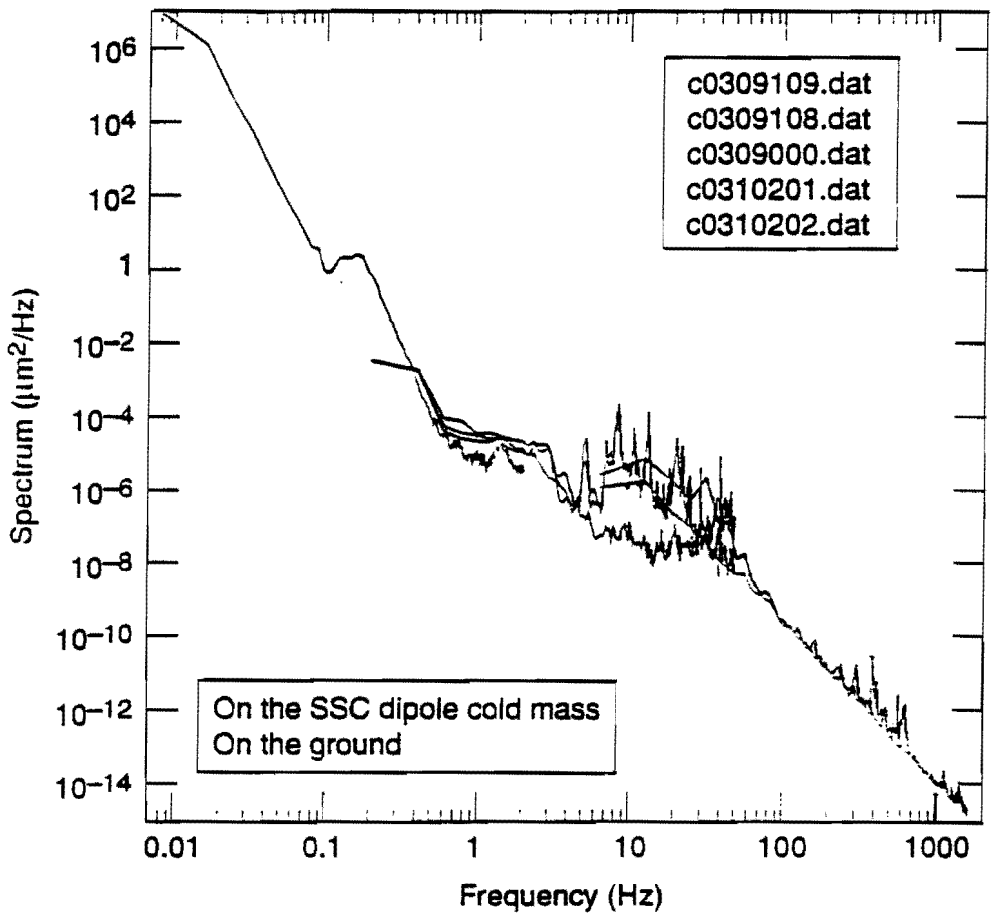

Figure 7.2 Measured spectral density of power of vertical vibrations in a very broad frequency band of 0.07-1720 Hz at the SSC site. From Ref. 16.

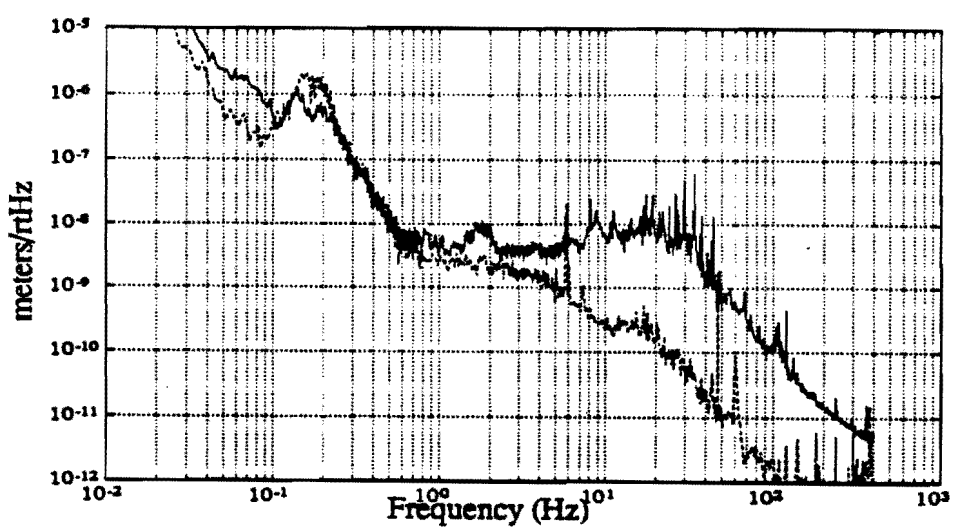

Figure 7.3 Measured spectral density of amplitude of vertical seismic motion. Solid curve is lab # B042 of JILA at the Univ. of Colorado, Boulder. Dashed curve is Building 8 of NIST,

interferometer due to a $\xi(f)$ of 3×10^{-9} m /$\sqrt{\text{Hz}}$ is $\Delta n/n \leq 1.3 \times 10^{-22}$ /$\sqrt{\text{Hz}}$. The motion contributes a noise that is 60% of the shot-noise limit of the proposed interferometer. Thus this is potentially an important noise source.

It is highly desirable if one can increase the frequency of modulation for the detected signal. For example, choosing f = 100 Hz will alleviate the problems associated with ground motion. However, this conflicts with the long storage time of the high finesse Fabry-Perot cavity. Nevertheless a compromise between finesse and modulation frequency should be possible, especially by using an asymmetric cavity in which the finesse is lower without sacrificing the sensitivity.

7.2.3. Recommendations Regarding Scattering

The calculations above show that scattered light can be a potentially dangerous limiting factor for the proposed experiment. Very carefully designed baffles are definitely needed to suppress as much as possible the scattered light from recombining into the main beam mode. A problem here is the small size of the SSC magnet bore diameter. There is not enough room to put in baffles of the optimal height for stray light suppression. A maximum baffle height of 0.9 cm can be used without introducing diffraction losses that are comparable to the mirror losses into the Gaussian beam mode of the propagating laser. As a first design, the first set of baffles would be placed at a distance of 10 m from the mirrors. Ideally, subsequent baffles should be placed at the anchor point of each magnet. This is to ensure that the motion of the baffles is controlled by the ground alone, and not by other effects such as ramping of the magnetic field. Again this may not be possible. The use of a liner as a distributed light scatterer/absorber looks promising and warrants serious consideration.

The above calculations are at best a rough estimate of what the scattering noise may be. We have not included the scattering due to the flexure motion of the interferometer, and we have ignored the different scattering probability of the two polarizations. Also we have not considered diffraction aided reflection off the baffle edges. Therefore it is imperative that a numerical

analysis of the stray light problems in the interferometer be carried out as early as possible. Programs such as APART and GUERAP could be employed to determine the phase noise that will be introduced due to ground or other motions. These Monte-Carlo programs will also allow for optimization of baffle or liner and light trap placements/configurations. As input to the numerical simulations, it will be necessary to know the amount of ground motion at the experimental site, the effect of magnet ramping, and the bidirectional scattering functions of the beam pipe and possible liner/light trap materials. These measurements related to the magnets, liner material and the experimental site should be made as soon as possible, to allow these parameters to be investigated in a timely manner. We have explored the possibility of doing such a calculation with BRO, Inc. in Tuscon, Arizona. The cost of a numerical calculation is on the order of $50,000. The high cost is associated with the need to calculate the two polarizations separately, while keeping track of extremely small phase differences due to very small beam pipe motions.

7.3 References

[1]. A. D. Buckingham, W. H. Prichard and D. H. Whiffen, Trans. Faraday Soc. (London) **63**, 34 (1967).

[2]. William Turner, private communication.

[3]. R. Cameron, et al., Phys. Lett. A **157**, 125 (1991).

[4]. V. Anashin et al., "Cold beam tube photodesorption and related experiments for the SSCL 20 TeV proton collider", SSCL Preprint-533, (March, 1994).

[5]. J. Gómez-Goñi, O. Gröbner and A. G. Mathewson, "Comparison of photodesorption yields using synchrotron radiation of low critical energies for stainless steel, copper and electrodeposited copper surfaces", to be published.

[6]. W. C. Turner, private communication.

[7]. W. C. Turner, "Dynamic vacuum in the beam tube of the SSCL collider - cold beam tube and liner options", SSCL-preprint-404, (May 1993).

[8]. T. Kobari and H. J. Halama, J. Vac. Sci. Tech. **5**, 2355 (1987).

[9]. *American Institute of Physics Handbook*, ed. Dwight E. Gray (McGraw Hill, 1957), page

6-91.

[10]. A. Abramovici et al., Science **256**, 325 (1992).

[11] Kip. S. Thorn, "Light scattering and proposed baffle configuration for the LIGO", January 1989, report #36 of list of 3/1/89.

[12]. V. V. Parkhomchuk, V. D. Shiltsev and H. J. Weaver, "Measurements of ground motion and SSC dipole vibrations", SSCL-preprint-624 (June 1993)

[13]. David B. Newell, "Six degree of freedom active vibration isolation at 1 Hz and above", Ph. D. thesis, Univ. of Colorado, Boulder (1994).

[14]. D. C. Agnew, "Strainmeters and tiltmeters", Rev. Geophys. **24**, p.579-624 (1986).

[15]. Kip S. Thorn, private communication.

8. EVALUATION OF PROJECT RISKS AND RISK MITIGATION

The technical risks associated with this experiment along with their proposed mitigation have been discussed in detail in the previous technical sections. The technical risk areas are summarized below. The numbers in parenthesis refer to the sections in which the risks are discussed.

Vacuum system

Risks

- Current magnet vacuum capability is inadequate for this experiment. (4.8)
- Beam tube vacuum degrades due to scattered light photodesorption of H_2 from the walls, leading to low operating cycle time between magnet warmups (7.1.1).
- Design of differential pumping to interface the optical chamber at pressure ~10^{-7} torr to the beam tube area at pressure of $\leq 10^{-12}$ torr (5.3)

Mitigation (4.8, 5.1, 7.7.1, 7.2)

- Add pump out ports in the interconnect region of the magnets.
- Use a liner to reduce photodesorption of physisorbed H_2 and as a distributed light baffle. to cut down the scattered light.
- Use cryosorber in the liner to help in pumping.
- Several stages of differentially pumped sections.

Scattered light

Risks

- Scattered light related to seismic motion introduces phase noise into the detected signal and degrades optical system measurement capability. (7.2)
- Scattered light causes photodesorption of H_2, thus degrading the beam pipe vacuum. (7.1.1)
- Motion of beam tube as a result of changing magnetic field impacts scattered light.

Mitigation (7.2.3)

- Careful design and placement of baffle and light traps.
- Use liner in the beam tube as distributed absorber.
- Use magnet interconnect pump out regions as light traps.
- Clean environment to maintain the low loss of the mirrors. (3.1)
- Perform Monte Carlo simulations for the system to properly evaluate the effect of beam pipe motion and to optimize baffle/light trap/absorber configuration.

Residual gas

Risks

- Directly related to the quality of vacuum.
- The Cotton-Mouton effect has a magnetically induced birefringence with the same signature as the desired signal. (7.1.1)
- Effective temperature of photodesorbed H_2 unknown. (7.1.1)

Mitigation

- Obtain as good a vacuum as possible in the beam tube region. Same risk mitigation as the vacuum system.
- Studies of photodesorption of H_2

Optical system

Risks

- Birefringence measurement at the 0.1% QED level requires unprecedented technical requirements in frequency metrology. (3.4)
- Motion of interferometer mirrors from seismic excitations prevents initial lockup of cavity. (3.4)

Mitigation

- Employ passive vibration isolation and active control of mirror motion (3.3, 3.4, 5.2)
- Proposed new scheme of birefringence measurement technique. (3.4).
- Proof of principle experiment is now under way (3.5).

Magnet system

Risks (discussed in section 4.8)

- Experiment requires ≥ 100 A/s ramp rate.
- Quench current dependence of ramping a system of two magnets has not been investigated.

Mitigation

- Evaluated single magnet performance to select "good" magnets for the experiment. (4.2)
- Assemble two magnet string for full system test to define operational envelop.
- Lower the temperature of the He into the magnets.
- Develop light baffle system. Same mitigation as scattered light.

9. SCHEDULE OF EXPERIMENT

9.1 Introduction

The proposed duration of the project is five years. The first three years of experiment will have parallel efforts under way at Colorado and at Fermilab. In Colorado a 3 m interferometer will be developed to allow perfecting the optical measurement system using a high-finesse Fabry-Perot cavity. At Fermilab the experimental area will be developed, power and cryogenics will be installed, photodesorption experiments will be performed, the vacuum system will be designed, and a vibration isolation system will be developed relevant to a 50 m interferometer. The optical system will be installed in the 50 m interferometer in the third year. The last two years are devoted to the actual measurements of the experiment.

Since there is considerable experience in the laser interferometer gravitational wave projects, the accelerator community, and in our collaboration on the other problems such as vibration isolation, laser stabilization, cavity locking, superconducting magnet operations, scattered light, and residual gas effects, we expect these areas to be only hurdles rather than impassable barriers. The potential background in the experiment which are of greatest concern are those which may be phase correlated with the magnet ramping. These include the Cotton-Mouton effect from photodesorbed H_2, light scattering changes associated with beam tube motion, and other sources which may not have been anticipated. A full test of these effects require the full magnet system, laser, and 50 m interferometer. These items are scheduled to be installed together in the third year.

Consequently, our plan is based on a direct attack on all major problems, including the design and construction of the optical, vacuum and vibration isolation system from early in the project. The major intermediate steps we will be taking are (1) an experimental study of photodesorption, (2) a series of tests with single magnets to find the optimum parameters of operation, and (3) extensive experience with a 3 meter Fabry-Perot interferometer at Colorado State/Colorado Universities before attempting to install a full 50 m interferometer at Fermilab.

Note that the 3 meter interferometer makes stringent tests of the optical, vacuum and vibration isolation systems to be used in the 50 m interferometer.

9.2 Yearly milestones

Prior to project:

Apply for funding from appropriate sources.

Define equipment (SSCL assets) to be requested for experiment.

Year 1:

Transport SSC equipment to Fermilab.

Conduct single magnet testing to determine operating parameters

Perform photodesorption studies

Magnetic enclosure made usable

Construct cryogenic system

Construct QPS

Design 50 m vacuum system

Design 50 m beam tube liner system

Design 50 m optical chambers and vibration isolation system

Establish 40 m test optics system

Initiate study to reduce scattered light in the beam tube from the mirrors.

Design 3 m interferometer

Design 3 m vacuum system

Evaluate performance of electro-optic birefringence measurement scheme.

Investigate performance of lock/servo electronics and suspended mirror control system.

Determine light scattering reduction requirements and method.

Determine effect of laser power on birefringence of the mirrors.

Year 2:

Complete physical plant for experiment

Install cryogenic system

Install magnet power system

Install QPS

Install control system

Construct beam tube liner system

Construct 50 m vacuum system

Construct optical chambers and vibration isolation system

Establish 40 m test interferometer

Construct 3 m vacuum system

Construct vacuum electro-optic birefringence spectrometer

Construct servo/lock electronics and suspended mirror control system.

Install 3 m interferometer.

Year 3:

Install magnets in experimental area.

Install 50 m vacuum system

Install 50 m optics chambers and vibration isolation system

Confirm performance of passive and active seismic isolation systems.

Characterize motion of magnets during ramping.

Investigate H_2 levels in the magnet bore tube and the effect of scattered light.

Test vibration isolation, stray light, and locking of the 3 meter interferometer.

Determine optical noise characteristics of birefringence measurement with the 3 meter interferometer.

Confirm performance of laser beam pointing control system.

Optical system moved to Fermilab

Year 4:

Install 50 m interferometer

Test vibration isolation, stray light, and locking of the 50 meter interferometer.

Begin initial experimental program using magnets and interferometer.

Study systematic noise sources and noise reduction techniques.

Measure initial QED signal.

Define any modifications to experimental setup.

Make any necessary equipment modifications.

Year 5:

Make precision measurement of QED effect.

Conduct axion search.

Define any future plans for experiment

10. DISTRIBUTION OF EFFORT AND COST ESTIMATES

This section represents the result of a bottom-up cost estimate of this experiment assuming a distribution of effort among the collaborators as given below. This estimate includes the basic assumptions that (1) duplication of effort within the collaboration will be minimized, (2) some well identified components will be available from the SSC and (3) maintenance of the non-optics part of the experiment would be provided by the Accelerator Division and Research Division of Fermilab on a non-high-priority basis.

10.1 Distribution of Responsibilities

10.1.1 Colorado State University & University of Colorado/JILA

The Colorado group will be responsible for the development of a 3 m Fabry-Perot laser interferometer and the birefringence and rotation measurement systems with a design goal of measuring the change in the index of refraction between two orthogonal polarizations of a beam of light with shot-noise limited sensitivity. This effort will be undertaken at these institutions under anticipated grants from NIST, NSF, and/or DOE. (See section 10.3.) After preliminary studies with the 3 m interferometer are complete, this optical system will be moved to Fermilab and integrated with the 50 m interferometer.

10.1.2 Fermi National Accelerator Laboratory

The Fermilab effort will be divided among the Accelerator Division, Research Division, and Physics Department. The Accelerator Division will be responsible for the experimental area at E-4R, installation of the two SSC dipole magnets, powering the magnets, supplying the cryogenics to cool the magnets, safety systems and the magnet and cryogenic control system. The Research Division will be responsible for the beam tube and optical chamber vacuum systems, beam tube light baffle system, beam tube liner and the optical vacuum chambers. The Physics Department will be responsible for supporting the research and development for the

active and passive vibration isolation systems, a rudimentary 50 m Fabry Perot cavity for vibration isolation studies, a study of photodesorption of H_2 by laser light, and a study of mirror birefringence. General operating support for the Fermilab experimental group will be requested from the AD, RD and PD in proportion to the related efforts in those divisions/departments.

It is anticipated that within the first two years the experimental area will become operational and a preliminary 50 m optical system will be established. Vibration studies in situ will lead to a vibration isolation system for the interferometer mirrors and magnets. Studies of photodesorption will lead to a beam tube liner and vacuum system satisfactory for the experiment. Light scattering tests and calculations will aid in the development of a beam tube light baffle system. In the third year the magnets will be installed in the interferometer. The Colorado optics will be installed at the end of the third year and initial debugging of the full 50 m interferometer will begin.

10.2 Cost Estimates

10.2.1 Colorado State University and University of Colorado/JILA

Personnel (man-months)		
Senior personnel	20	
Postdocs	156	
Graduate students	348	
Technician	12	
TOTAL PERSONNEL COST (K$)		1294
(includes fringe, tuition and 45% indirect cost)		
Equipment (K$)		
Optical interferometer	546	
Vacuum system	347	
Vibration isolation	168	
TOTAL EQUIPMENT COST		1061
Operating costs (K$)		
M & S ($40K/yr.)	290	
Travel	113	
TOTAL OPERATING COST		403
(includes 45% indirect cost)		
TOTAL COLORADO STATE/COLORADO COST (K$)		**2758**

10.2.2 Fermi National Accelerator Laboratory

Fermilab Accelerator Division

General operating $10K/year

CRYOGENICS DEPARTMENT

	Plant $K	M&S $K	EDIA mm	Tech mm	Prog. mm	SSC Items
Transfer lines (45 m)		50		3		
Transfer line feed can		40		3		
Transfer line return can		60	3	3		
Magnet feed cans (two)				1		
U tubes						
Gas buffer tank		25		1		
Quench header		5		1		
Instrumentation		10		2		
TOTAL CRYOGENICS DEPT.		190	3	14		

ELECTRICAL DEPARTMENT

	Plant $K	M&S $K	EDIA mm	Tech mm	Prog. mm	SSC Items
QPMs		25	0.1	1.2	1.5	
Controls					1	
Voltage to frequency converters		10	0.3	0.8		
Heater Firing Units		3	0.4	0.8		5 HFU
UPSs --- Use TEV Spares---		1.6		0.2		
Power Supply --Use MI R&D Supply--			0.5	0.5	0.3	
Controls		6	0.5	1		
TOTAL ELECTRICAL DEPT.		46	1.8	4.5	2.8	

MECHANICAL DEPARTMENT

	Plant $K	M&S $K	EDIA mm	Tech mm	Prog. mm	SSC Items
						(3) 15 m dipole magnets
Magnet bus (220 ft.)		24	1			
Magnet moving to E-4R		9	0.7	0.4		magnet trailer
Survey			0.1	0.1		
Magnet connections inc. end boxes		10	3.5	2.5		cryostat cutters cryostat parts
TOTAL MECHANICAL DEPT.			43	5.3	3.0	

ACCELERATOR CONTROLS GROUP

	Plant $K	M&S $K	EDIA mm	Tech mm	Prog. mm	SSC Items
System controls inc. application page		10		2		

EXPERIMENTAL PHYSICAL PLANT

	Plant $K	M&S $K	EDIA mm	Tech mm	Prog. mm	SSC Items
Optics house #1 20'x20' class 10,000 with heat and cooling and power @ $250/ft^2	100		2			
Optics house #2 15'x15' class 10,000 with heat and cooling and power @ $250/ft^2	56		1			
Magnet enclosure - Seal, insulate, heat, and cool	25		1			
TOTAL PLANT	181		4			

Fermilab Research Division

General operating $10K/year

	Plant $K	M&S $K	EDIA mm	Tech mm	Prog. mm	SSC Items
Beam tube high vacuum system		65	2	4		
Beam tube liner system		15	1	2		
Beam tube light baffle system		20	1	3		
Optics towers vacuum system		65	2	4		
Optics towers vacuum enclosure		100	2	4		
Use of Class 10 Clean Room				1		
TOTAL RESEARCH DIVISION		265	8	18		

Fermilab Physics Section

General operating $20K/year

	Plant $K	M&S $K	EDIA mm	Tech mm	Prog. mm	SSC Items
Interferometer						
Nd:YAG laser 532 nm, 400 mW		25				
Stabilization/filter cavity		10				
Interferometer mirror set		8				
Optical modulators & misc. optics		25				2 tables
Locking electronics & remote drives		12		4		
Vibration Isolation						
1st Stage Vibration Isolation 2x15		30	2	3		
2nd Stage Vibration Isolation 2x15		30	2	3		
Inertial Platform 2x20		40	2	3		
Feedback sensors and electronics		25	2	3		
Photodesorption Studies						
Residual Gas Analyzer		15				
Control and DAQ Computer		10		1		
TOTAL PHYSICS SECTION		230	8	17		

TOTAL FERMILAB COST

Plant $K	M&S $K	EDIA mm	Tech mm	Programmers mm
181	784	30	59	3

10.2.3 Total Experiment Cost (K$)

Colorado State University/University of Colorado	**2758**
Fermilab	**965**
TOTAL EXPERIMENT COST (K$)	**3543**

10.3 Funding Options for the Colorado State/Colorado Costs

The groups from Colorado State University (CSU) and University of Colorado (CU) have submitted a proposal (2/27/95) to the National Science Foundation Academic Research Infrastructure Program, for the development of the 3 m interferometer. The proposal went through internal review at CSU and was selected by CSU for commitment of matching funds. The request to NSF is $696 K. If funded, Colorado State University has agreed to match the full amount of the NSF grant, making the total $1392 K. This would cover all of the estimated equipment costs ($1061 K) and the portion of the personnel costs specifically associated with interferometer development and construction.

A pre-proposal was also submitted by S. A. Lee (1/31/95) to the National Institute of Standards and Technology 1996 Precision Measurements Grant Program. This pre-proposal has now been selected as one of five finalists to compete for two awards, with the final proposal due in May of 1995. The Precision Measurements Grant carries an award of $50 K per year, for three years for a total of $150 K.

If the NSF Infrastructure proposal, with CSU matching, and the NIST proposal are funded, the remaining personnel and operating costs of the experiment, totalling $1215 K, would have to be obtained from other sources. Pending the approval of the proposed experiment by Fermilab, the Colorado groups plan to submit additional proposals to the National Science Foundation and the Department of Energy to cover these costs. The average request per year would be $243 K /yr.

The funding of the NSF Infrastructure proposal, with CSU matching, is obviously a very critical component of the CSU/CU funding plan. The NIST Precision Measurement Grant proposal, although only covering a small portion of the total costs, is also very important. Should the Infrastructure proposal not be funded, a NIST grant would allow the Colorado collaborators to construct a simplified and less ambitious test interferometer, with which many of the critical concepts of the experiment could be tested and demonstrated, and important results obtained. If the Infrastructure proposal is funded, a NIST grant would provide immediate support for initiating the research effort, while the NSF grant supports the equipment development. The NIST grant is therefore particularly critical for initiating the experiment in a timely fashion.